Dynamics and Chemistry of Marine Stratocumulus – DYCOMS-II

Bjorn Stevens[1][2] Donald H. Lenschow[b], Gabor Vali[c], Hermann Gerber[d], A. Bandy[#], B. Blomquist[#],
J.-L. Brenguier[†], C. S. Bretherton[⋆], F. Burnet,[†], T. Campos[b], S. Chai[††], I. Faloona[b], D. Friesen[b],
S. Haimov[c], K. Laursen[b], D. K. Lilly[⋆], S. M. Loehrer[§], Szymon P. Malinowski[x], B. Morely[b],
M. D. Petters[c], D. C. Rogers[b], L. Russell[¶], V. Savic-Jovcic[2], J. R. Snider[c], D. Straub[y], Marcin
J. Szumowski[††], H. Takagi[c], D.C. Thorton[#], M. Tschudi[b], C. Twohy[z], M. Wetzel[††], M. C. van Zanten[2]

ABSTRACT

The second Dynamics and Chemistry of Marine Stratocumulus (DYCOMS-II) field study is described.
The field program consisted of nine flights in marine stratocumulus West-Southwest of San Diego California.
The objective of the program was to better understand the physics and dynamics of marine stratocumulus.
Toward this end special flight strategies, including predominantly nocturnal flights, were employed to optimize estimates of entrainment velocities at cloud top, large-scale divergence within the boundary layer, drizzle processes in the cloud, cloud microstructure, and aerosol-cloud interactions. Cloud conditions during
DYCOMS-II were excellent with almost every flight having uniformly overcast clouds topping a well-mixed
boundary layer. Although the emphasis of the manuscript is on the goals and methodologies of DYCOMS-II, some preliminary findings are also presented — the most significant being that the cloud layers appear to
entrain less and drizzle more than previous theoretical work led investigators to expect.

[1]*Corresponding Author Address:* Bjorn Stevens, Department of Atmospheric Sciences, University of California Los Angeles,
405 Hilgard Ave., Box 951565, Los Angeles, CA 90095-1565. Email: bstevens@atmos.ucla.edu.

[2]Department of Atmospheric Sciences, University of California Los Angeles, Los Angeles California, USA; [b]National Center
for Atmospheric Research, Boulder Colorado, USA; [c] Department of Atmospheric Science, University of Wyoming, Laramie
Wyoming, USA; [d]Gerber Scientific Inc., Reston, Virginia, USA; [#]Department of Chemistry, Drexel University, Philadelphia,Pennsylvania, USA; [†]CNRM Meteo-France, Toulouse Cedex, France; [⋆] Department of Atmospheric Sciences, University
of Washington, Seattle Washington, USA; [††]Desert Research Institute, Reno Nevada, USA; [⋆]School of Meteorology, University of
Oklahoma, Norman Oklahoma, USA; [§]Joint Office for Science Support, University Corporation for Atmospheric Research, Boulder Colorado, USA; [x]Institute of Geophysics, Warsaw University, Warsaw Poland; [¶]Princeton University, Princeton New Jersey,
USA; [y]Department of Atmospheric Science, Colorado State University Ft. Collins Colorado, USA; [z]College of Oceanography and
Atmospheric Sciences, Oregon State University, Corvallis Oregon, USA.

The stratocumulus topped boundary layer (hereafter the STBL), which prevails in the subtropics in regions where the underlying ocean is much colder than the overlying atmosphere, is thought to be an important component of the climate system. Perhaps most striking is its impact on the radiative balance at the top of the atmosphere. The seasonally averaged net cloud radiative forcing from the STBL has been estimated to be as large as 70 Wm^{-2} (Stephens and Greenwald, 1991), more than an order of magnitude larger than the radiative forcing associated with a doubling of atmospheric CO_2. This means that even rather subtle sensitivities of the STBL to changes in the properties of the atmospheric aerosol (cf., Twomey, 1974; Albrecht, 1989; Brenguier et al., 2000b), or the large-scale environment (Rodwell and Hoskins, 2001), can still project significantly onto the overall radiative budget. In addition, the effect of the STBL on the surface energy budget and thus the overall climatology of the tropics is also thought to be significant (cf., Mechoso et al., 1995; Ma et al., 1996; Philander et al., 1996). However, attempts to quantify these, and other, effects are frustrated by our inability to quantify, let alone understand, key elements of stratocumulus physics.

Two questions stand out: First, how efficiently do stratocumulus entrain (incorporate through turbulent mixing) air from the warm, dry, quasi-laminar, free troposphere, into the cool, moist, turbulent boundary layer? Second, how important is drizzle? The two processes are, of course, related. Both act directly to reduce the amount of water in the cloud layer, and indirectly to modify the heat budget, thereby impacting the dynamics. Moreover, because drizzle is thought to suppress entrainment (Stevens et al., 1998), and because entrainment is thought to suppress drizzle, the relative interplay between the processes may be subtle, which could make them difficult to untangle. Nonetheless, recent advances in observational technology have introduced new possibilities for understanding entrainment, drizzle, their interplay, and external processes (such as factors regulating cloud microstructure, and cloud-aerosol interactions) which may regulate this interplay. This combination of refined theoretical questions, and advances in observational technologies, helped to motivate a recent field program, DYCOMS-II (Dynamics and Chemistry of Marine Stratocumulus) which this paper aims to describe.

Entrainment

To help one understand why entrainment is so important it helps to think in terms of the mixed layer theory of Lilly (1968), wherein the STBL is identified as a distinct layer of the atmosphere whose properties are largely determined by exchanges with the underlying surface on the one hand, and dilution through the incorporation of air from the free-troposphere (i.e., entrainment) on the other. The entrainment velocity, E can be defined in terms of an equation for the depth, h, of the STBL:

$$\frac{dh}{dt} = E + W_h, \tag{1}$$

where W_h is the large-scale vertical velocity evaluated at h. One can think of E as the diabatic growth rate of the layer. It essentially quantifies the dilution rate of the STBL and thus is critical in determining its overall state.

Interest in entrainment is not only motivated by its importance to the state of the STBL, but also by the extent to which previous work has been unable to constrain it. Indeed much recent work has been devoted toward articulating an entrainment rule, which given the mean state and the forcing would produce an estimate of E. Most of this work has been based on large-eddy simulation. It has, in part, been spurred on by the startling results of Moeng and co authors (1996), which show how simulations of the same case by different groups differ by nearly an order of magnitude in their prediction of the mixing (or entrainment) rate across cloud top. Such differences have subsequently been shown to be due to a variety of factors, most notably variability in the treatment of physical processes such as radiation and condensation. But numerical issues are also important, Stevens et al. (1999) show that insufficient resolution of the radiative

cooling in the vicinity of the cloud top interface leads to systematic biases in estimates of entrainment. More unified treatments of physical processes have helped reduce the discrepancies among models, but (perhaps because of poorly understood numerical sensitivities) significant differences persist. In a survey of recent work Stevens (2002) shows that different entrainment rules derived from state-of-the-art simulations can still differ by more than a factor of two. Moreover, when these parameterizations are incorporated into a mixed-layer model, the equilibrium solutions for typical climatological conditions have equilibrium sensible and latent heat fluxes that vary by as much as 40 Wm^{-2} and cloud liquid water paths that vary by factors of two or more. With this degree of discord, one might think that observations could usefully arbitrate disputes posed by models. However, estimating entrainment from real data has also proven to be challenging.

Fundamentally there are two different techniques for inferring E from data, we call these the divergence and tracer method respectively. The divergence method evaluates E from (1) as:

$$E = \frac{dh}{dt} + \int_0^h \mathcal{D} dz, \tag{2}$$

where $\mathcal{D} = \partial u/\partial x + \partial v/\partial y$ is the divergence of the horizontal wind. The tracer method evaluates E from the budget of trace-constituents (denoted by c) across the cloud top interfacial layer. If this layer is sufficiently thin, and if sources of c are not important over this region, the budget requires that

$$E \approx \frac{(\overline{w'c'})_h}{c_+ - \overline{c}}, \tag{3}$$

where $(\overline{w'c'})_h$ is the turbulent flux just below the top of the cloud layer. The term in the denominator, often referred to as the jump and denoted Δc, measures the change in the constituent amount across the top of the STBL. Note that the number of independent estimates of E which can be deduced from the tracer method is only limited by ones ability to identify and measure tracers, c, with suitable properties, i.e., well defined jumps and negligible interfacial sources. Moreover, because $(\overline{w'c'})_h$ can be estimated independently in two ways (either directly via eddy-correlation, or as a residual of the budget of c over the STBL as a whole), to the extent that the numerator in (3) is the source of uncertainty in the estimate of E, one can estimate E in two independent ways for each tracer.

In the past it has not been possible to estimate $\mathcal{D}$ from flight data in the STBL, and so investigators who have tried to use the divergence method, i.e., (2), for estimating E have been forced to rely on forecast models for estimates of $\mathcal{D}$, (e.g., Bretherton et al., 1995; De Roode and Duynkerke, 1997). As a consequence most previous estimates of E have been based on an application of the tracer method. For instance during DYCOMS-I (Lenschow et al., 1988) entrainment was estimated on the basis of fast response measurements of O_3 and H_2O (Kawa and Pearson, 1989). Likewise, in his studies of stratocumulus over the North Sea Nicholls (1984) estimated E based on the water budget. Subsequent studies, (e.g., Bretherton et al., 1995; De Roode and Duynkerke, 1997) have made similar estimates, either based on measurements of O_3 or water vapor. Despite the growing literature, previous observations have not provided particularly strong bounds on E. One reason is that neither H_2O nor O_3 are ideal tracers for estimating entrainment, so that estimates based on an application of the tracer method using these variables tend to have relatively large uncertainties. Another reason is that almost all observational estimates of entrainment have been for daytime, when the radiative forcing of the boundary layer is difficult to measure and changes considerably with time. In contrast, all of the theoretical work applies to nighttime, which eliminates these complications.

DYCOMS-II addressed these issues by sampling the clouds predominantly at night, and by attempting to estimate E using both the divergence and tracer methods. In addition to better constraining the forcing, nighttime measurements eliminate solar forcing (which is difficult to measure) and thus facilitates estimates of the heat budget. Because the evolution of cloud base couples the heat and moisture budgets of the

layer, simply tracking the evolution of cloud base during the night greatly constrains these budgets, thereby constraining heat or moisture budget based estimates of entrainment using (3).

During DYCOMS-II, tracer based estimates of E were also based on measurements of two additional passive tracers, DMS (CH_3SCH_3 or dimethyl sulfide) and Ozone (O_3). In these cases the numerator in (3) was estimated only from eddy correlation measurements, as budget residual estimates were more difficult to make. The use of DMS in this regard is novel. Because the only known source of DMS is at the surface, and because its lifetime (a few days) is too short to lead to appreciable concentrations in the free atmosphere but is long compared to the mixing timescale in the STBL, it should exhibit well defined jumps. For this reason it is thought to be nearly ideal for estimating entrainment via (3). In contrast H_2O and O_3 can vary significantly above the boundary layer, leading to large uncertainties in estimates of the jumps, which frustrates the use of (3) to estimate E. Indeed O_3 sometimes has jumps that change sign across the study area (e.g., Kawa and Pearson, 1989), thereby making the relation (3) ill defined. Another limitation of H_2O is that it is partitioned into two phases in the cloud layer, this makes it difficult to measure on the one hand, and introduces gravitational fluxes out of air parcels (drizzle), which behave in a non-conservative manner, on the other hand. DYCOMS-II hoped to at least overcome the measurement difficulties of H_2O in the cloud through the use of a new, high-rate, laser hygrometer (the TDL, or tunable diode laser, May, 1998) capable of making very precise measurements of water vapor in cloud. Although in principle DMS has more potential as a means for estimating entrainment, the idea was not to supplant the other tracer based methods of estimating E, but rather to supplement them with an additional tracer-based method of comparable or greater accuracy.

DYCOMS-II also was designed around the possibility of estimating E using the divergence method. To do so requires a means for estimating $\mathcal{D}$, and the evolution of h. Technological advancements which make this feasible include the development of the Scanning Aerosol Back-scatter Lidar (SABL) and the GPS-corrected wind fields. The SABL gives precise measurements of cloud-top height when flying above cloud. GPS corrections to the gust-probe plus inertial reference system estimates of the wind motivate estimates of $\mathcal{D}$ by integrating the track normal component of the lateral velocity field around a closed flight track (Lenschow, 1996; Lenschow et al., 1999). The mean vertical velocity at the STBL top may then be estimated as $-\mathcal{D}h$. In addition, proxy data from forecast models, and estimates of $\mathcal{D}$ directly from remotely sensed wind fields (e.g., SeaWinds, Liu, 2002), and the tracking of layers in composite soundings from dropsondes, all provide additional constraints and bounds on the method, thereby increasing our ability to evaluate E from (2).

One last technological development which motivated a new observational attack on the entrainment problem was the availability of the NSF/NCAR C130. Its long-range facilitates more extensive sampling of more remote layers, and its large-payload enables the delivery of a greater range of scientific instrumentation to the target area.

The Flights

The field program took place in July 2001. Remotely sensed data, forecast model output, and other data of opportunity were collected and archived for the entire month, and research flights took place from July 7, 2001 through July 28, 2001. Flight operations were based out of North Island Naval Air Station, just across the bay from San Diego. The target area was approximately one hour west southwest of San Diego as illustrated in Fig. 1. The field program consisted of seven entrainment research flights and two radar research flights.

The entrainment flights were designed following a template illustrated with the aid of Fig. 2. Although no single flight followed this schematic exactly, its essential elements were incorporated into every entrainment flight. These elements included circles to estimate divergences and fluxes concurrently (see also the
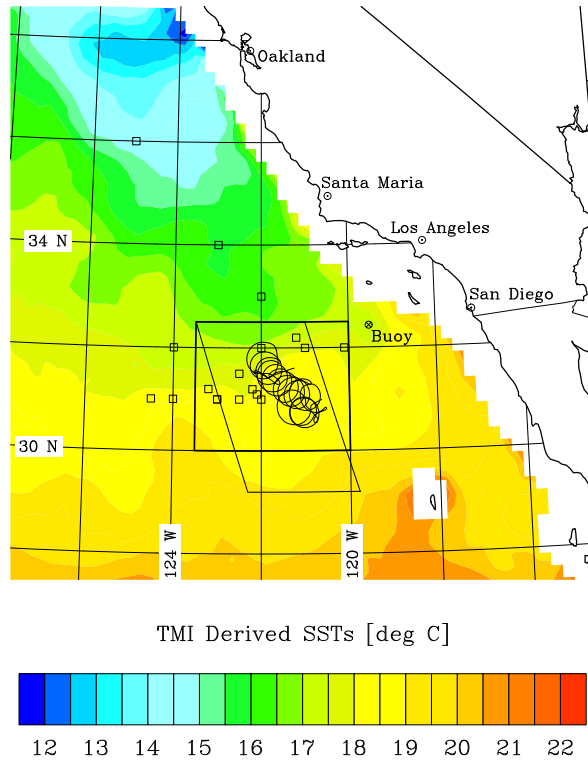
Figure 1: DYCOMS-II target area superimposed on TMI derived SSTs for the experimental period [the TRMM (Tropical Rainfall Measurement Mission) Microwave Imager (TMI), sees through non precipitating cloud decks]. The planned target area (for which forecast data is archived) is shown by the rectangle. The actual target area, where 90-95% of the measurements were made (excluding ferries) is shown by the rhomboid. Flight track RF07 is also overlaid to illustrate a typical entrainment flight pattern. Open boxes are approximate locations of previous flights during DYCOMS-I and eight of the ten FIRE flights. The location of the Tanner Banks Buoy is also noted.

flight track in Fig. 1) and long legs to reduce sampling errors in fluxes and other higher-order statistics. The stacking of these legs can allow better estimates of cloud-top or surface fluxes. In addition, frequent profiling of the layer facilitated evaluation of the layer evolution. Lastly, the long legs above cloud allowed ample time for remote sampling of the layer.
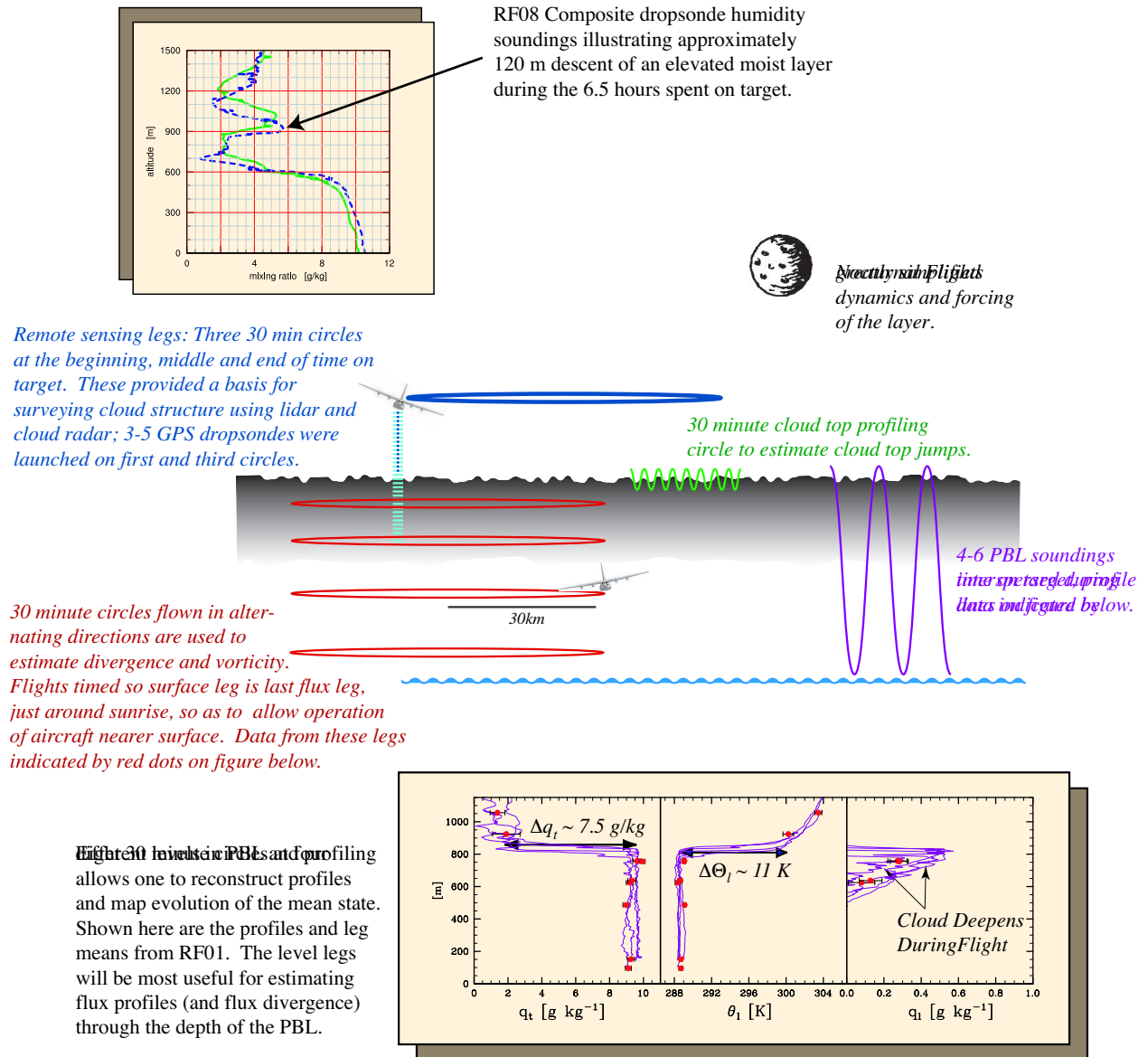

RF08 Composite dropsonde humidity soundings illustrating approximately 120 m descent of an elevated moist layer during the 6.5 hours spent on target.

Nocturnal flights *dynamics and forcing of the layer.*

Remote sensing legs: Three 30 min circles at the beginning, middle and end of time on target. These provided a basis for surveying cloud structure using lidar and cloud radar; 3-5 GPS dropsondes were launched on first and third circles.

30 minute cloud top profiling circle to estimate cloud top jumps.

4-6 PBL soundings interspersed during profile data indicated by below.

30 minute circles flown in alternating directions are used to estimate divergence and vorticity. Flights timed so surface leg is last flux leg, just around sunrise, so as to allow operation of aircraft nearer surface. Data from these legs indicated by red dots on figure below.

30km

Different levels in circles and profiling allows one to reconstruct profiles and map evolution of the mean state. Shown here are the profiles and leg means from RF01. The level legs will be most useful for estimating flux profiles (and flux divergence) through the depth of the PBL.

$\Delta q_t \sim 7.5$ g/kg

$\Delta \Theta_l \sim 11$ K

Cloud Deepens DuringFlight

Figure 2: DYCOMS-II Flight Strategy. Symbols in bottom panel refer to total water mixing ratio, q_t, its change across cloud top, Δq_t, liquid water potential temperature θ_l, its change across cloud top, $\Delta \theta_l$, and liquid water mixing ratio q_l.

Experimental conditions during DYCOMS-II were excellent. The uniformity and extent of cloud cover were unprecedented, even for stratocumulus experiments. An example of the morning satellite imagery for RF01 is given in Fig. 3 — if anything the areal extent of the cloud layer was less on this flight than on subsequent flights. We attribute the favorable conditions to two factors: First, seven of nine research flights were nocturnal, and satellite images often showed that daytime gaps in the cloud layer tended to fill

during the early evening — well before our usual take-off time of around 11:15 pm local time. Second, the synoptic environment was more conducive to well-formed stratocumulus than usual. In past experiments it has been customary to rank cases, based on uniformity of cloud cover. For instance during DYCOMS-I Lenschow et al. (1988) developed a seven point scale for rating cloud cover, with one denoting solid, unbroken stratus, two near solid, with occasional breaks and three to seven denoting increasingly broken or more variable boundary layers. Although DYCOMS-I experienced generally more ideal conditions than subsequent large experiments (e.g., Albrecht et al., 1988, 1995) only one of the DYCOMS-I flights rated a one on the Lenschow scale, with three other flights rating a two. In contrast eight of the nine DYCOMS-II flights rated a one. The lone deviant was RF02 which had only 97% lidar-derived cloud cover and thus rated a two.

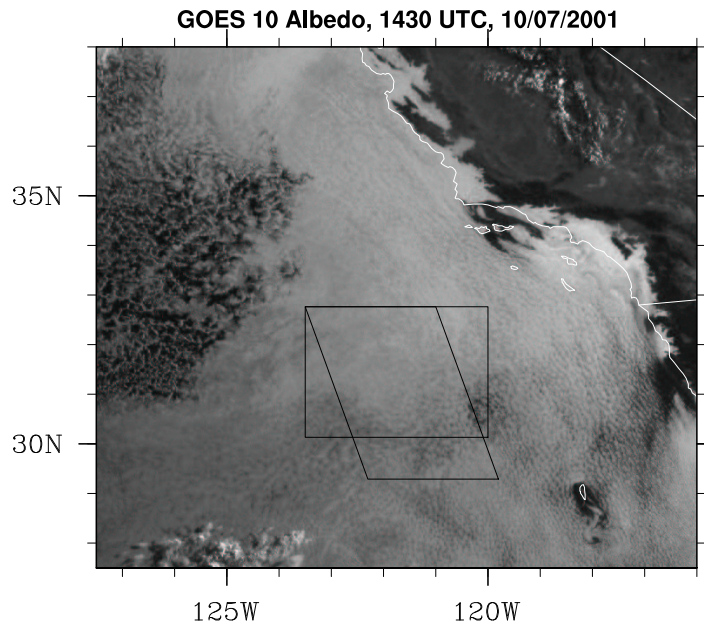**GOES 10 Albedo, 1430 UTC, 10/07/2001**

Figure 3: GOES 10 channel one (visible) image for conditions near the end of research flight (RF) 01. Note widespread region of uniform marine stratocumulus cloud cover surrounding the target area. The preliminary target area is boxed, the actual region in which almost all of the flight hours were spent is bounded by the rhomboid.

Apart from the uniformity of cloud cover, the structure of observed cloud layers varied greatly. Boundary layer depths varied by nearly a factor of two (from lows of 600 m on several of the flights to a high of 1100 m on RF04). Cloud depths, and cloud top liquid water concentrations varied similarly, with cloud depths ranging from less than 300 to over 500 m and liquid water concentrations from 0.5 - 1.0 $g\,kg^{-1}$. In contrast, DYCOMS-I also experienced relatively well-formed stratus layers, but the cloud depths were thinner, between 100 and 300 m. Surface winds during DYCOMS-II were generally northwesterly but their magnitude varied considerably, from 5 to 12 ms^{-1}. Microphysically we also observed rich differences in cloud structure, with some cloud layers having small numbers of cloud droplets, characteristic of a pristine marine environment, and others having somewhat larger concentrations of cloud droplets, indicative of a greater continental influence. Drizzle was common, with some flights showing persistent radar echos greater than 20 dBZ. Further details and a more quantitative overview of the flights are provided in the electronic supplement to this article. The variety of conditions sampled should enable an evaluation of how different aspects of the mean state influence the dynamics and physics of the cloud layer.

Much of the variability in cloud conditions correlates with variations in synoptic conditions. During the second week of flight operations (corresponding to Research Flights 4 through 6), the Pacific high strengthened and its major axis became oriented along a more north-south direction. At the same time a strong low pressure system developed off the coast of British Columbia, centered over Seattle at 00 UTC on 17 July. The influence of this depression was felt over the target area at upper levels and was associated with strong cold-air advection aloft. The 850 hPa temperature decreased by 8 K through the month and by 4 K through the first week of the experiment. These changes resulted in significantly weaker inversions and generally deeper (800-1100m) boundary layers with more variability in cloud-top height through the course of a given mission.
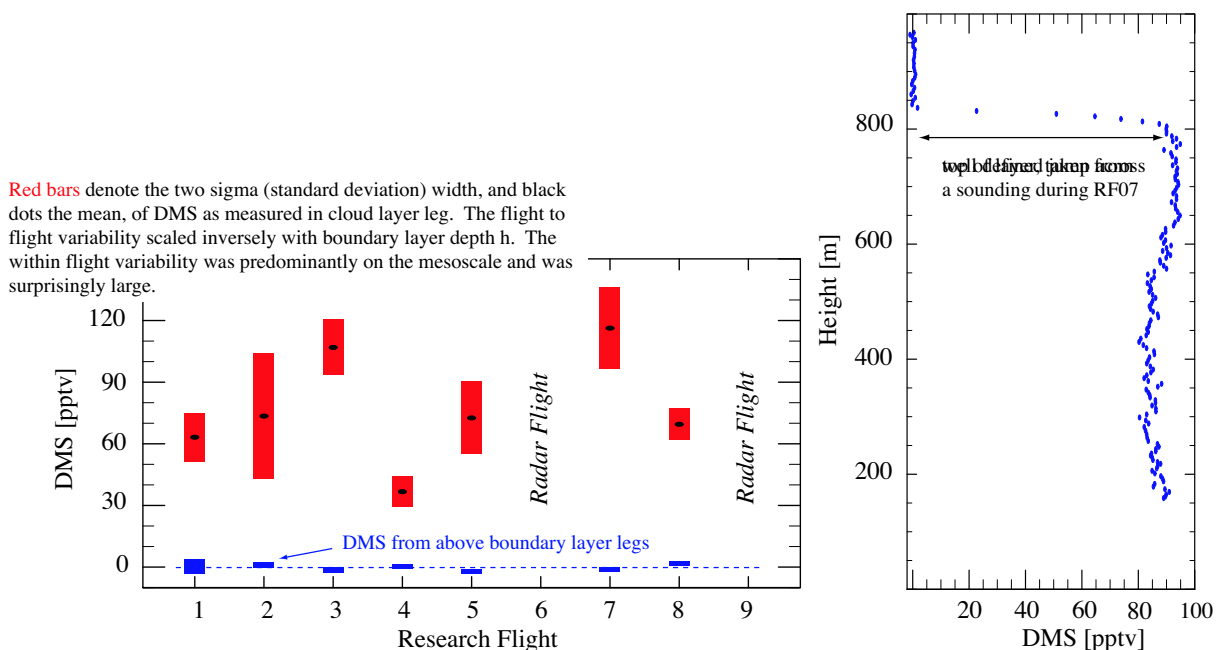

Figure 4: DMS Concentrations from Entrainment Flights.

Large flight-to-flight variability is also apparent in DMS concentrations (Fig. 4). DMS is rather more dilute when the boundary layer is deep (RF04 and RF05) and rather more concentrated when the boundary layer is shallow (RF03). Unlike some other tracers, DMS also varied considerably within a flight. As we had hoped, DMS existed in ample amounts on every leg within the STBL, but was effectively absent above, leading to well defined jumps locally. However we were surprised to routinely see DMS variations exceeding 20% around flight circles in the STBL. Such pronounced variability remains something of a mystery.

Drizzle

Few dispute that in regions where drizzle occurs, it is a key component of the water budget and can have an important impact on the dynamics and structure of the STBL. However, its role in the climatology of clouds on larger scales is controversial. Previous field programs have suggested that drizzle might be a relatively common phenomenon (e.g., Brost et al., 1982; Duynkerke et al., 1995; Fox and Illingworth, 1997; Vali et al., 1998), and thus could play a vital role in the evolution of the STBL (e.g., Paluch and Lenschow, 1991). In this respect simple theoretical models (e.g., Albrecht, 1989; Ackerman et al., 1993; Wang and Albrecht, 1986; Pincus and Baker, 1994) suggest that the modulation of drizzle by changes in the atmospheric

aerosol could regulate cloud amount and thickness. Because these ideas provide a straightforward mechanism whereby human activity could affect cloudiness, they have attracted considerable attention. Although there exists a modest and growing literature on drizzle in the STBL (e.g., Chen and Cotton, 1987; Wang and Wang, 1994; Austin et al., 1995; Gerber, 1996; Stevens et al., 1998; Vali et al., 1998) some very elementary questions remain, including the actual precipitation rates in marine stratocumulus and their relation to ambient aerosol, cloud thickness and intensity of turbulence. For this reason, a central element of the DYCOMS-II was an evaluation of drizzle processes in stratocumulus.
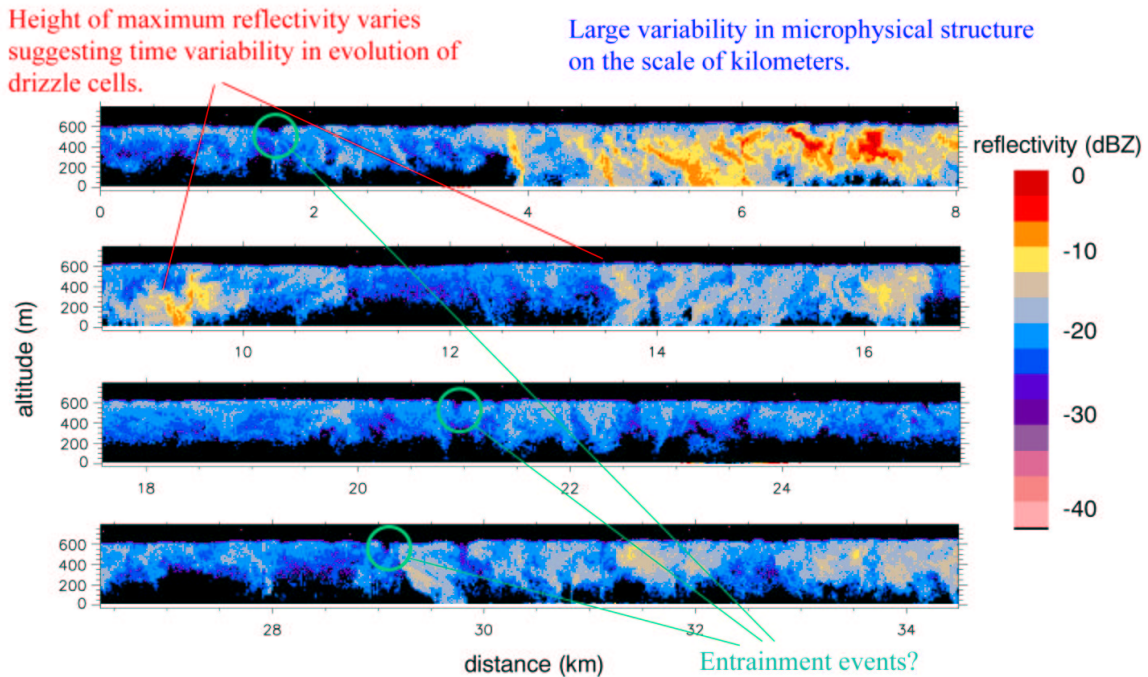

Figure 5: Radar reflectivity for a segment of research flight 3. The axis scales are 1:1.

The tendency toward less drizzle during the daytime, evidence of large spatial and temporal variability, and suggestions of considerable vertical structure have all frustrated attempts to quantify its role. In the past these problems were compounded by an exclusive reliance on *in situ* probes, whose sampling statistics are poor and whose measurements, because of the intermingling of spatial and temporal variability, are difficult to interpret. Cloud radars, on the other hand, sample much larger volumes, can rapidly profile an entire column (or layer depending on their orientation) and are sensitive to larger moments of the droplet spectrum. Thus they seem like a natural way to study drizzle. For this reason the University of Wyoming Cloud Radar (WCR) was mounted on the NSF/NCAR C130 for DYCOMS-II.

The WCR was mounted in the rear of the aircraft and alternately looked through two antennae, one that pointed straight down, and one that looked down and rearward (see electronic supplement). The DYCOMS-II flight strategy, with cloud and subcloud legs, allows comparison of *in situ* microphysical probe data with the radar reflectivity data from just below the aircraft to calibrate reflectivity/rainrate relationships for each of the flights. Above-cloud legs allowed one to image the entire STBL and thus yield a more complete view of the spatial structure of precipitation. Because the near surface region was always seen by the radar, reflectivity/rainrate relationships for a given flight can be used to estimate the mean precipitation flux at the

surface over the nearly seven hours during which the aircraft was in the study area, thus allowing much improved estimates of the role of drizzle during DYCOMS-II.
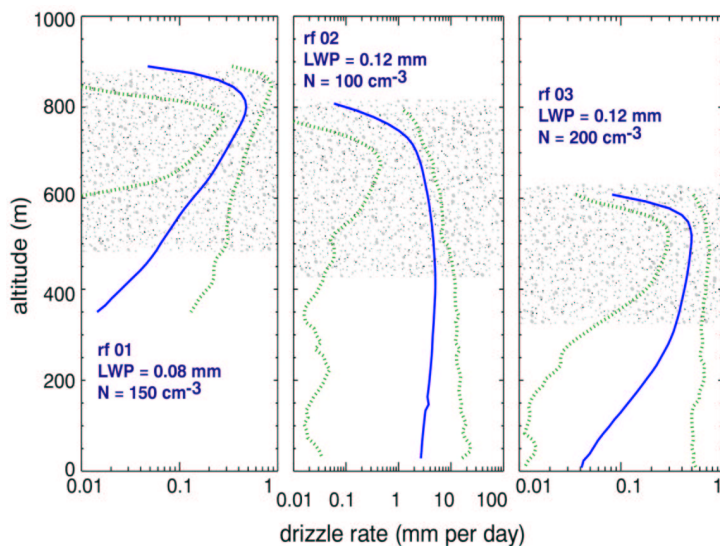

Figure 6: Vertical profiles of precipitation rates estimated from the Wyoming Cloud Radar data from research flights 1, 2 and 3. Stippled regions show the cloud layer. The blue lines are mean values for entire circles of about 200 km circumference. The dashed lines show the variability (90paths (LWP) and droplet concentrations (N) are also mean values.

The use of two antennae also made dual-Doppler analyses possible. Thus in addition to revealing the amount of drizzle in the STBL, and its local structure, the radar also images the velocity field in the cloud — particularly in weakly or non-precipitating regions where the Doppler signal is dominated by air-motions rather than the fall speeds of drizzle drops, which can be of a similar magnitude. In regions where drizzle is heavier, a variety of techniques are available to separate the fallspeed contribution from the air motion contribution to the Doppler velocity fields.

Two additional flights (RF06 and RF09) followed completely different patterns designed to evaluate the fine-scale structure and evolution of convective eddies within the cloud layer. Rather than large sweeping patterns designed to evaluate fluxes and budgets, RF06 and RF09 used staccato legs and sharp turns which returned the aircraft to a selected point in the flow along a variety of headings (see electronic supplement). This provides further insight into the interaction between microphysical and dynamical processes on the cloud scale, as well as a basis for comparing clouds observed during DYCOMS-II to those observed in previous campaigns (Vali et al., 1998) which used similar flight strategies.

As an example of the WCR data (Fig. 5) the structure of the cloud layer along a segment of RF03 shows considerable variability in reflectivity associated both with individual turbulent updrafts and downdrafts a few hundred meters wide and with mesoscale modulation on scales of 5 km or more. The variability in this 15 minute flight segment foreshadows the variability among flights. Some flights sampled much more drizzle than this, some almost none. One of the remarkable impressions left on the investigators was how the apparent uniformity of the cloud top viewed from above could mask enormous variations in the microphysical structure within the cloud layer.

Intra- and inter-flight variability is hinted at in Fig. 6, where averaged reflectivities are converted into rainrate profiles using relationships from previous field campaigns (Vali et al., 1998). Along with the mean profiles, profiles from sub-segments illustrate the variability within the layer. Combined with Fig. 5 a picture emerges whereby drizzle is clearly a convective, rather than a stratiform process, with drizzle rates in

localized regions being orders of magnitude larger than elsewhere in the cloud. Layer averaged drizzle rates greater than 0.5 mm/day (which correspond to evaporation rates of about 15 Wm^{-2}) begin to have significant effects on the layer averaged energetics. Local drizzle fluxes, which can be as large as 20 mm/day, would be expected to dominate the dynamics of circulations in their vicinity. In these cases the data suggest that drizzle helps organize the flow in a manner which helps maintain the cloud layer in the presence of drizzle, as there is circumstantial evidence that these regions of intense drizzle are remarkably persistent.

Cloud Microstructure

Beyond the elementary issue of simply quantifying the propensity of stratocumulus to drizzle, the question arises as to what underlying physical processes regulate drizzle fluxes to begin with. The characteristics of the cloud layers observed during DYCOMS-II can be compared to previous observations (e.g., Austin et al., 1995; Gerber, 1996) by comparing cloud droplet number concentrations, N, and cloud thickness. Initial indications are that the clouds observed during DYCOMS-II are somewhat thicker than the clouds that have been observed in this geographic region in the past. Observed clouds (see electronic supplement for a more detailed summary) ranged from less than 300 to over 500 m in depth, as compared to previous (mainly daytime) observations, where cloud depths tended to be between 150 and 300m. While the cloud layers observed during DYCOMS-II had more cloud condensation nuclei (CCN) than some of the drizzling layers observed during studies elsewhere, (e.g., the Atlantic Stratocumulus Transition Experiment), they were clearly characteristic of maritime clouds, with concentrations ranging from less than 100 to around 300 cm^{-3}.

Although the cloud microstructure is thought to influence, and in turn be influenced by, drizzle, might it not also tell us something about entrainment? Our discussion of entrainment above focused exclusively on entrainment rates; but what about entrainment processes — about which even less is known. The mixing of free-tropospheric air into the boundary layer requires warm-dry air parcels to mix with cool-saturated air parcels. Because warming and drying tend to evaporate cloud water the detailed cloud microphysical structure can serve as an excellent indicator of mixing processes at cloud top. However, in this case one is likely to be less interested in average droplet concentrations or liquid water contents than in the details of the deviations from these averages. To investigate such details from the C130 requires instrumentation capable of sampling the flow at a very high rate.

To address these issues an ultra-fast thermometer (the UFT, Haman et al., 1997), a fast forward-scattering spectrometer probe (the FFSSP, Brenguier et al., 1998) capable of estimating the droplet distribution, and a particle volume monitor (PVM, Gerber, 1994) for estimating liquid water, were mounted within six meters of each other (see electronic supplement and Fig 12) on the left wing of the C130. These probes all sampled the flow at rates of 1000 Hz or greater, thereby allowing one to explore the microphysical and thermodynamic structure of the cloud layer on scales ranging from 10 cm to several m. It is expected that the data from these instruments will provide a first look at the smallest scales and microphysical changes associated with the entrainment process at cloud-top (see for example Fig. 7).

The Aerosol

One aspect of the drizzle puzzle that human activities are known to influence is the background atmospheric aerosol, which regulates cloud droplet concentrations (N) and the average cloud microstructure. Largely for this reason, increasing attention is being given to quantifying relationships between the aerosol and stratocumulus microphysics. Some general rules regarding the relationship between aerosol properties (e.g., cloud condensation nuclei, CCN, or accumulation mode aerosol concentrations) and N (Erlick et al., 2001)
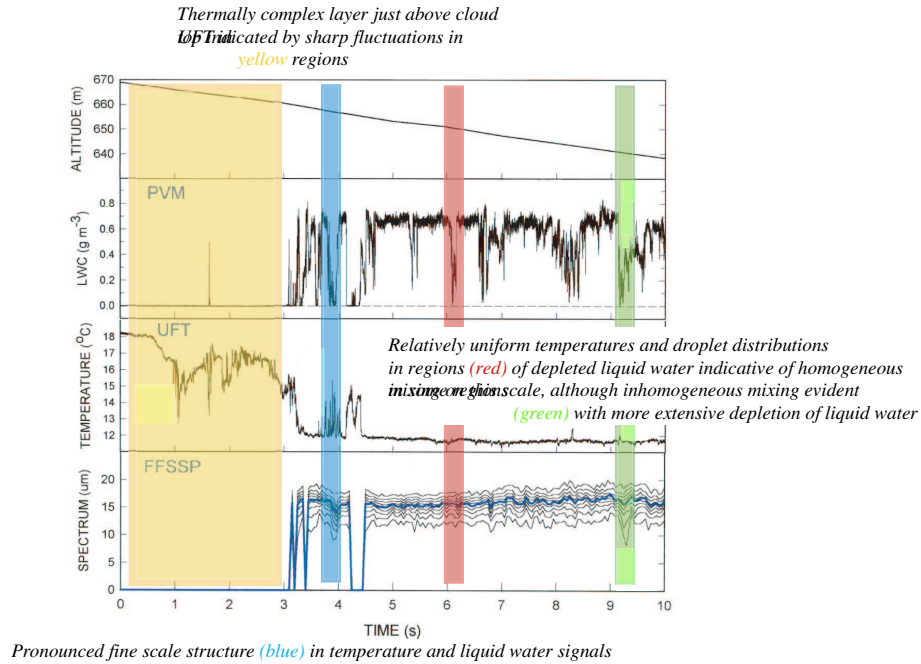
Thermally complex layer just above cloud top indicated by sharp fluctuations in yellow regions

Relatively uniform temperatures and droplet distributions in regions (red) of depleted liquid water indicative of homogeneous mixing on this scale, although inhomogeneous mixing evident (green) with more extensive depletion of liquid water

Pronounced fine scale structure (blue) in temperature and liquid water signals

Figure 7: Comparison of PVM, UFT and FFSSP ultra high-rate measurements during the flight of the NSF/NCAR C-130 through the top of an unbroken layer of Sc on 12 July (start of the 10-s interval is 12:05:38 UTC).

and to some extent drizzle formation (e.g., the review by Schwartz and Slingo, 1996) have been reported, but a comprehensive, physically based description of the aerosol and its impact on cloud microphysical processes remains outstanding.

Evaluations of the relationship between the CCN and N, by integrating parcel models over trajectory ensembles (e.g., Snider and Brenguier, 2000), reveal consistency between predicted and observed values of N; but that agreement may reflect compensating biases in the measurements of vertical velocity, CCN or N. The redundancy of the DYCOMS-II measurements of vertical velocity (C130 gust-probe and possibly Doppler velocities from the WCR), two independent estimates of CCN spectra and two estimates of N (from the SPP-100 and the Fast FSSP-100) should provide a more definitive test. Reflectivity measurements from the WCR are also providing an improved means for selecting non-precipitating cloud regions for conducting these types of analyses.

Assuming consistency between the CCN and N can be established, attention can be focused on what is thought to be the more vexing problem (cf., Fig. 8)–specifically, how to relate the measured characteristics of the aerosol to the CCN, or alternatively N. Although the theory of Köhler (e.g., Rogers and Yau, 1989) links aerosol and cloud properties, its application is complicated by the difficulty in properly accounting for the complexity of actual aerosol composition or the competing effects of particles in polluted conditions (Bigg, 1986; Russell et al., 1999; Charlson et al., 2001). Most recently ACE-2 investigators have documented discrepancies of up to a factor of two between concentration calculated following the Köhler theory and CCN measurements (Raes et al., 2000; Brenguier et al., 2000a). One source for observed discrepancies could be sizing biases in the measurements. Bias in the CCN spectrum might result from overestimates of the applied supersaturation in the CCN chamber. For the aerosol spectrum, sizing biases could result from interpreting the measurements of morphologically complex particles as if they had been ideal, homogeneous
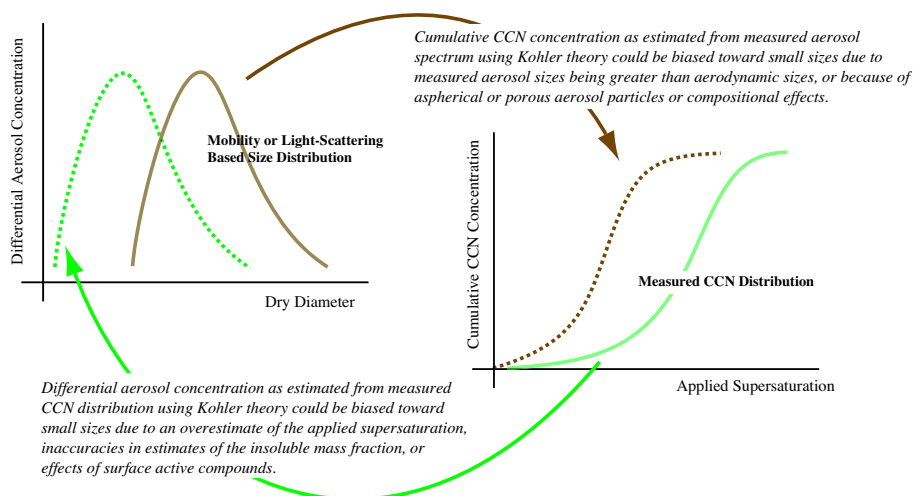
Figure 8: Illustration of the relationship between the dry aerosol size spectrum and the CCN distribution, and the problems that can occur in attempting to relate one to the other.

spheres. An alternative hypothesis is that chemical components, such as organic compounds, are altering the surface tension, solubility, and water uptake due to mixture nonidealities neglected by the classical theory. DYCOMS-II provided the opportunity to address possible sizing biases or compositional effects with complementary techniques.

Sizing biases in the aerosol spectrum as measured during DYCOMS-II are being evaluated in a number of ways. First, the size distribution is a blending of data from a variety of instruments, i.e., a scattering spectrometer probe (SPP-300) measures particles from 0.3-20 μm diameter; a passive cavity aerosol spectrometer (SPP-200) measures particles 0.1-3 μm diameter; and a radial differential mobility analyzer (RDMA) measures particles 0.01-0.1 μm diameter.[3] These measurements are being compared to redundant condensation nuclei counters (which measure the total aerosol concentration). Second, *in situ* estimates of the aerosol size distribution are being compared to distributions derived from microscopic sizing of the aerosol impacted on a filter. Last, a diffusion battery is being used to compare size-segregated measurements of CCN and total aerosol concentrations, (e.g., Gras, 1990).

Composition effects on the activation spectrum of the aerosol spectrum are also being investigated using DYCOMS-II data. The composition of the subcloud aerosol is being determined from an analysis of individual particles as well as from bulk samples collected on filters during subcloud flight legs. Electron microscopy (e.g., Pósfai et al., 1999) of individual aerosol particles is providing qualitative information on elemental composition, complemented by bulk filter analysis using X-ray fluorescence for elements and Fourier transform infrared spectroscopy for functional groups — thus providing an opportunity to examine both external mixing of different types of particles and the role of organics (Maria et al., 2002). To better understand the detailed composition of that component of the subcloud aerosol that is actually activated into cloud droplets, a counterflow virtual impactor (Twohy et al., 2001) was flown during DYCOMS-II to collect individual droplet residual particles after evaporation. These residual particles are being analyzed similarly to the subcloud aerosol. Additional compositional information is being provided by an experimental cloud water collector (Straub et al., 2001) which allows the quantification of pH, inorganic ions, and total organic carbon in cloud droplets residing at different levels in the cloud. These latter techniques, which look at the composition of cloud droplets, can also lend insight into the modification of aerosol composition through repeated cycles of activation and evaporation of cloud droplets.

---

[3]See the electronic supplement for a more complete description of the particle-sizing probes.

Summary and Speculation

A recent field program, DYCOMS-II, was conducted in the stratocumulus regime of the Northeast Pacific. In roughly descending order of emphasis DYCOMS-II strove to answer four questions: (i) What is the entrainment rate? (ii) How much does it drizzle? (iii) What is the nature of cloud microphysical variability on sub-meter scales? (iv) Can the activation spectrum of cloud droplets be understood based on measurements of the atmospheric aerosol?

To answer these questions DYCOMS-II made use of novel instrumentation and flight strategies. These included nocturnal flights, which integrated remote sensing (cloud radar, lidar, radiometers, and dropsondes) and *in situ* data collection (using standard turbulence and thermodynamic probes as well as an enhanced suite of mircrophysical instrumentation) from a single airborne platform. In addition a new method for making fast measurements of atmospheric DMS was employed to study entrainment mixing. Overall DYCOMS-II brought together a large suite of instrumentation capable of describing the dynamics, chemistry and physics of the stratocumulus topped boundary layer over an unprecedented range of scales. DYCOMS-II also benefitted from the good fortune of extraordinarily cooperative meteorology; conditions were ideal on every flight. Such a combination of favorable meteorology and extensive instrumentation can be expected to produce as many surprises as answers. In this respect some puzzles to emerge from initial analyses of the data include: the origins of remarkably large variability in boundary layer DMS, and mechanisms for sustaining persistent regions of very strong drizzle.

In addition to the emerging puzzles, in closing it also seems fitting to outline at least some of the preliminary findings which are being explored with great interest — even if so doing involves some degree of extrapolation from the data presented above. Broadly speaking, the finding with perhaps the widest implications is that stratocumulus appear to entrain less and drizzle more than previously thought. For instance, during RF01 (see Fig. 2) the cloud top interface was unstable by many measures, yet the cloud appeared to thicken substantially during the course of the flight. Preliminary analyses also indicate a remarkable degree of correspondence among various tracer-based estimates of entrainment, all of which produce entrainment rates of order $0.4 \, \mathrm{cm \, s^{-1}}$ which is significantly smaller than what is predicted by many current parameterizations. Indeed preliminary attempts to apply parameterized entrainment relations to the observed cloud layers generally result in a marked thinning of the layer.

The extent of drizzle observed during DYCOMS-II is consistent with entrainment drying of the cloud layer being rather inefficient, but is nonetheless remarkable. On some flights preliminary estimates of drizzle rates at the surface over large areas and long time periods averaged near a millimeter per day. Even on flights where relatively little drizzle reached the surface, drizzle fluxes at cloud base could be pronounced. Indeed, the canonical picture of "non-precipitating marine stratocumulus" was rather more rare than common, suggesting that drizzle might indeed be a key element of the dynamics of the STBL. Although conclusions such as the above are necessarily speculative they do provide the promise that the DYCOMS-II data will teach us fundamentally new things, and thus whet the appetite for further investigation.

References

Ackerman, A. S., O. B. Toon and P. V. Hobbs, 1993: Dissipation of marine stratiform clouds and collapse of the marine boundary layer due to the depletion of cloud condensation nuclei by clouds. *Science*, **262**, 226–229.

Albrecht, B. A., 1989: Aerosols, cloud microphysics and fractional cloudiness. *Science*, **245**, 1227–1230.

Albrecht, B. A., C. S. Bretherton, D. Johnson, W. S. Schubert and A. S. Frisch, 1995: The Atlantic stratocumulus transition experiment – ASTEX. *Bull. Amer. Meteor. Soc.*, **76**, 889–904.

Albrecht, B. A., D. A. Randall and S. Nicholls, 1988: Observations of marine stratcumulus clouds during FIRE. *Bull. Amer. Meteor. Soc.*, **69**, 618–626.

Austin, P., Y. Wang, R. Pincus and V. Kujala, 1995: Precipitation in stratocumulus clouds: Observational and modeling results. *J. Atmos. Sci.*, **52**, 2329–2352.

Bigg, E. K., 1986: Discrepancy between observation and prediction of concentrations of cloud condensation nuclei. *Atmospheric Research*, **20**, 82–86.

Brenguier, J.-L., T. Bourrianne, A. de Araujo Coelho, R. Jacques Isbert, Robert Peytavi, D. Trevarin and P. Weschler, 1998: Improvements of droplet distribution size measurements with the fast-FSSP (forward scattering spectrometer probe). *J. Atmos. Oceanic Tech.,*, **15**, 1077–1090.

Brenguier, J.-L., P. Y. Chuang, Y. Fouquart, D. W. Johnson, F. Parol, H. Pawlowska, J. Pelon, L. Schüller, F. Schröder and J. R. Snider, 2000a: An overview of the ACE-2 CLOUDYCOLUMN closure experiment. *Tellus*, **52B**, 814–826.

Brenguier, J.-L., H. Pawlowska, , L. Schuüller, R. Preusker, J. Fischer and Y. Fouquart, 2000b: Radiative properties of boundary layer clouds: Droplet effective radius versus number concentration. *J. Atmos. Sci.*, **57**, 803–821.

Bretherton, C. S., P. Austin and S. T. Siems, 1995: Cloudiness and marine boundary layer dynamics in the ASTEX lagrangian experiments. part II: Cloudiness, drizzle, surface fluxes, and entrainment. *J. Atmos. Sci.*, **52**, 2724–2735.

Brost, R. A., J. C. Wyngaard and D. H. Lenschow, 1982: Marine stratocumulus layers. Part II: Turbulence budgets. *J. Atmos. Sci.*, **39**, 818–836.

Charlson, R. J., J. H. Seinfeld, A. Nenes, M. Kulmala, L. A. and F. M. C., 2001: Atmospheric science - reshaping the theory of cloud formation. *Science*, **292**, 2025–2026.

Chen, C. and W. R. Cotton, 1987: The physics of the marine statocumulus-capped mixed layer. *J. Atmos. Sci.*, **44**, 2951–2977.

De Roode, S. R. and P. G. Duynkerke, 1997: Observed Lagrangian transition of stratocumulus into cumulus during ASTEX: mean state and turbulence structure. *J. Atmos. Sci.*, **54**, 2157–2173.

Deardorff, J. W., 1972: Parameterization of the planetary boundary layer for use in general circulation models. *Mon. Wea. Rev.*, **100**, 93–106.

Duynkerke, P. G., H. Zhang and P. J. Jonker, 1995: Microphysical and turbulent structure of nocturnal stratocumulus as observed during ASTEX. *J. Atmos. Sci.*, **52**, 2763–2777.

Erlick, C., L. M. Russell and V. Ramaswamy, 2001: Microphysics-based investigation of the radiative effects of aerosol-cloud interactions for two MAST experiment case studies. *J. Geophys. Res.*, **106**, 1249–1270.

Fox, N. I. and A. J. Illingworth, 1997: The retrieval of stratocumulus cloud properties by ground-based cloud radar. *J. App. Meteor.*, **36**, 485–492.

Gerber, H., 1994: New microphysics sensor for aircraft use. *Atmospheric Research*, **31**, 235–252.

Gerber, H., 1996: Microphysics of marine stratocumulus clouds with two drizzle modes. *J. Atmos. Sci.*, **53**, 1649–1662.

Gras, J., 1990: Cloud condensation nuclei over the southern ocean. *Geophy. Res. Let.*, **17**, 1565–1567.

Haman, K. E., A. Makulski and S. P. Malinowski, 1997: A new ultrafast thermometer for airborne measurements in clouds. *J. Atmos. Oceanic Tech.,*, **14**, 217–227.

Kawa, S. R. and R. Pearson, Jr, 1989: An observational study of stratocumulus entrainment and thermodynamics. *J. Atmos. Sci.*, **46**, 2649–2661.

Lenschow, D. H., 1996: A proposal for measuring entrainment into the cloud-capped boundary layer. in *Proc. ETL/CSU cloud-related process modeling and measuremetn workshop*, pp. 29–55. NOAA/ETL, Boulder, CO.

Lenschow, D. H., P. B. Krummel and S. T. Siems, 1999: Measuring entrainment, divergence, and vorticity on the mesoscale from aircraft. *J. Atmos. Oceanic Tech.,*, **14**, 1384–1400.

Lenschow, D. H., I. Paluch, A. Bandy, R. Pearson, Jr, S. R. Kawa, C. J. Weaver, B. Huebert, J. G. Kay, D. C. Thorton and A. R. Driedger, 1988: Dynamics and chemistry of marine stratocumulus (DYCOMS) experiment. *Bull. Amer. Meteor. Soc.*, **69**, 1058–1067.

Lilly, D. K., 1968: Models of cloud topped mixed layers under a strong inversion. *Quart. J. Roy. Meteor. Soc.*, **94**, 292–309.

Liu, W. T., 2002: Progress in scatterometer application. *J. Oceanography*, **58**, 121–136.

Ma, C.-C., C. R. Mechoso, A. W. Robertson and A. Arakawa, 1996: Peruvain stratus clouds and the tropical Pacific circulation. *J. Climate*, **9**, 1635–1645.

Maria, S. F., L. M. Russell, B. J. Turpin and R. Porcja, 2002: Elemental and functional group composition during PELTI. *Env. Sci. Tech.*

May, R. D., 1998: Open-path, near-infrared tunable diode laser spectrometer for atmospheric measurements of H_2O. *J. Geophys. Res.*, **103**, 19,161–19,172.

Mechoso, C. R., A. W. Robertson, N. Barth, M. K. Davey, P. Delecluse, P. R. Gent, S. Lneson, B. Kirtman, M. Latif, H. LeTreut, T. Nagai, J. D. Neelin, S. G. H. Philander, J. Polcher, P. S. Schopf, T. Stockdale, M. Suares, L. Teray, O. Thual and J. J. Tribbia, 1995: The seasonal cycle over the tropical Pacific in coupled ocean-atmosphere general circulation models. *Mon. Wea. Rev.*, **123**, 2825–2838.

Moeng, C.-H. and co authors, 1996: Simulation of a stratocumulus-topped PBL: Intercomparison among different numerical codes. *Bull. Amer. Meteor. Soc.*, **77**, 261–278.

Nicholls, S., 1984: The dynamics of stratocumulus: Aircraft observations and comparisons with a mixed layer model. *Quart. J. Roy. Meteor. Soc.*, **110**, 783–820.

Paluch, I. R. and D. H. Lenschow, 1991: Stratiform cloud formation in the marine boundary layer. *J. Atmos. Sci.*, **48**, 2141–2157.

Philander, S. G. H., D. Gu, D. Halpern, G. Lambert, N.-C. Lau, T. Li and R. Pacanowski, 1996: Why the ITCZ is mostly north of the equator. *J. Climate*, **9**, 2958–2972.

Pincus, R. and M. B. Baker, 1994: Effect of precipitation on the albedo susceptibility of marine boundary layer clouds. *Nature*, **372**, 250–252.

Pósfai, M., J. Anderson, P. R. Buseck and H. Sievering, 1999: Soot and sulfate aerosol particles in the remote marine troposphere. *J. Geophys. Res.*, **104**, 21,685–21,693.

Raes, F., T. Bates, F. McGovern and M. van Liedekerke, 2000: The 2nd Aerosol characterization experiment (ACE-2): General overview and main results. *Tellus*, **52B**, 111–125.

Rodwell, M. J. and B. J. Hoskins, 2001: Subtropical anticyclones and summer monsoons. *J. Climate*, **14**, 3192–3211.

Rogers, R. R. and M. K. Yau, 1989: *A short course in cloud physics*. International Series in Natural Philosophy. Butterworth Heinemann, Woburn MA, third edition, 290 pages.

Russell, L. M., J. H. Seinfeld, R. C. Flagan, R. J. Ferek, D. H. Hegg, P. V. Hobbs, W. Wobrock, A. Flossmann, C. D. O'Dowd, K. E. Nielsen and P. A. Durkee, 1999: Aerosol dynamics in ship tracks. *J. Geophys. Res.*, **104**, 31077–31096.

Schwartz, S. E. and A. Slingo, 1996: Enhanced shortwave cloud radiative forcing due to anthropogenic aerosols. in P. J. Crutzen and V. Ramanathan, editors, *Clouds, Chemistry and Climate*. Springer-Verlag, Berlin.

Snider, J. R. and J.-L. Brenguier, 2000: A comparison of cloud condensation nuclei and cloud droplet measurements obtained during ACE-2. *Tellus*, **52B**, 828–842.

Stephens, G. L. and T. J. Greenwald, 1991: The Earth's radiation budget and its relation to atmospheric hydrology. 2. Observations of cloud effects. *J. Geophys. Res.*, **96**, 15,325–15,340.

Stevens, B., 2002: Entrainment in stratocumulus mixed layers. *Quart. J. Roy. Meteor. Soc.*, in press, available from http://www.atmos.ucla/˜bstevens/publications.html.

Stevens, B., W. R. Cotton, G. Feingold and C.-H. Moeng, 1998: Large-eddy simulations of strongly precipitating, shallow, stratocumulus-topped boundary layers. *J. Atmos. Sci.*, **55**, 3616–3638.

Stevens, B., C.-H. Moeng and P. P. Sullivan, 1999: Large-eddy simulations of radiatively driven convection: sensitivities to the representation of small scales. *J. Atmos. Sci.*, **56**, 3963–3984.

Straub, D., J. L. Collett, Jr., D. Baumgardner and R. Friesen, 2001: Design and characterization of a new airborne cloudwater sampler. in *Proceedings of the 2nd International Conference on Fog and Fog Collection, St. John's Newfoundland, Canada*, pp. 209–212, Boston MA. American Meteorological Society.

Twohy, C. H., J. G. Hudson, S. S. Yum, J. R. Anderson, S. K. Durlak and D. Baumgardner, 2001: Characteristics of cloud nucleating aerosols in the Indian Ocean region. *J. Geophys. Res.*, **106**, 28699–28710.

Twomey, S. A., 1974: Pollution and the planetary albedo. *Atmos. Environ.*, **8**, 1251–1256.

Vali, G., R. D. Kelly, J. French, S. Haimov, D. Leon, R. E. McIntosh and A. Pazmany, 1998: Finescale structure and microphysics of coastal stratus. *J. Atmos. Sci.*, **55**, 3540–3564.

Wang, S. and B. A. Albrecht, 1986: A stratocumulus model with an internal circulation. *J. Atmos. Sci.*, **43**, 2374–2390.

Wang, S. and Q. Wang, 1994: Roles of drizzle in a one-dimensional third-order turbulence closure model of the nocturnal stratus-topped marine boundary layer. *J. Atmos. Sci.*, **51**, 1559–1576.

Appendix: Data[4]

Because of the enormous amount of data collected during DYCOMS-II, much of it from instruments developed and operated by individual investigators, an important component of the experimental strategy is the development of a proper archive. This is even more pressing when one considers the amount of relevant data available from space based platforms, the subjective opinions of on site observers, and other sources of opportunity. To identify and collect data in the latter category, investigators worked with JOSS (the joint office for scientific support, which operates as part of the University Corporation for Atmospheric Research) to develop an online field catalog which provided centralized access to information and data relating to all aspects of the field operations. This catalog included various textual reports (e.g. weather forecasts and aircraft flight summaries); a number of imagery products that were either produced by JOSS (e.g. high resolution satellite images and loops), produced by DYCOMS-II scientists (e.g. specialized model products), or gathered from various Internet sources (e.g. oceanographic analyses from the Naval Oceanographic Office); and finally information on each of the aircraft missions (e.g. take-off and landing times, flight tracks, dropsonde data, etc). The catalog was used in the field for operations and planning support as well as allowing scientists not in the field to follow the progress of the project. It was also a useful tool after the completion of the field phase to help determine cases for analysis.

After the field phase the field catalog was blended with other sources of data not available in real time (ranging from aircraft data to satellite radiances) to form the DYCOMS-II data archive. This archive provides distributed access to all of the operational and research data-sets collected during the project. It will continue to grow as various processed products are added to it. For instance simulations which attempt to synthesize the observed cases may later be incorporated into the archive. Both the catalog and the archive are available to all via the DYCOMS-II Data Management web page (http://www.joss.ucar.edu/dycoms). They provide a natural starting point for researchers interested in DYCOMS-II data sets which we hope will be extensively used.

Inset 1: Entrainment[5]

To illustrate how entrainment helps regulate the state of the STBL we begin with the equation describing the evolution of the bulk (layer averaged) value of a horizontally homogeneous conserved scalar, $\bar{c}$, in a marine layer of some depth h:

$$\frac{d\bar{c}}{dt} = \frac{(\overline{w'c'})_0 - (\overline{w'c'})_h}{h}. \tag{4}$$

Here $(\overline{w'c'})_0$ is the flux of c evaluated at the surface, and $(\overline{w'c'})_h$ is the entrainment flux, i.e., the turbulent flux of c estimated at the top of the layer. The surface flux $(\overline{w'c'})_0$ can be evaluated using similarity theory: $\overline{w'c'}_0 = C_d \|\mathbf{U}\|(c_s - \bar{c})$ where C_d is an exchange coefficient, c_s is the value of the scalar at the surface, and $\mathbf{U}$ is the vector wind (e.g., Deardorff, 1972). If the entrainment zone is sufficiently thin the entrainment flux can (in analogy to the surface flux) be linearly related to the entrainment velocity $E : (\overline{w'c'})_h = -E(c_+ - \bar{c})$ (e.g., Lilly, 1968; Stevens, 2002). Here c_+ is the value c takes just above the boundary layer. The depth of the layer h also depends on E following:

$$\frac{dh}{dt} = E + W_h, \tag{5}$$

W_h being the large-scale vertical velocity evaluated at the top of the layer. If the divergence, $\mathcal{D}$, of the mean horizontal wind is constant with height, $W_h = -\mathcal{D}h$. In steady-state the time-derivatives in both (4) and (5)

---

[4]To appear in print version of article

[5]This material will appear outside of the main text of the article, sort of like a boxed inset

vanish leading to the following relations for the equilibrium values of $\overline{c}$ and h :

$$\overline{c} = \frac{C_d\|U\|c_s + Ec_+}{C_d\|U\| + E}, \quad \text{and} \quad h = \frac{E}{\langle \mathcal{D} \rangle}. \tag{6}$$

Here $\langle \mathcal{D} \rangle$ denotes the bulk divergence within the boundary layer. Because boundary layer total-water specific-humidity, q_t and the liquid-water static-energy $s_l = c_p T + gz - Lq_l$ (the enthalpy variable), behave to a first approximation like conserved scalars, the above relations illustrate the critical role of E not only in determining the budgets of arbitrary scalars, but also in determining the mean thermodynamic state of the boundary layer and its depth. This latter information in turn determines other climatologically important quantities, such as cloud amount — or surface fluxes.

Inset 2: Secondary DYCOMS-II Objectives[6]

The basic scientific objectives, and in particular the seven entrainment flights, also permitted a number of secondary objectives as highlighted below.

NIGHTTIME REMOTE SENSING

The DYCOMS-II program has provided a unique opportunity for evaluating and improving night-time satellite remote sensing techniques, when the commonly used shortwave reflectance information is not available and while radiative forcing is controlled by thermal processes. The effects of nocturnal longwave cooling on cloud physics and dynamics also play an important role in the subsequent impacts of solar heating during the day. Little research has been conducted on night-time multispectral satellite analysis techniques, and refinement of these methods could provide significant input to mesoscale forecasting methods. Due to the reduced information content of satellite observations at night, it is imperative that mesoscale model diagnostic and prognostic products be optimally combined with the remote sensing data. Field studies such as DYCOMS-II are thus needed for development of multi-component data assimilation methods. Both geostationary and polar-orbiting satellite platforms were utilized to obtain research data for DYCOMS-II. The NOAA Geostationary Operational Environmental Satellite (GOES) is an essential source of information for determining temporal evolution of oceanic stratocumulus. Design improvements and better data distribution for geostationary satellite systems are making global near-continuous observations a reality, so that analysis techniques developed from DYCOMS will be applicable to other regions of persistent stratocumulus. New polar-orbiter satellites such as the NASA Terra platform have less frequent time sampling, but provide higher spatial and spectral resolution that will aid in detailed testing of retrieval methods. The 15-minute temporal resolution of GOES-West satellite data is being utilized for interpretation of cloud field evolution as the C-130 aircraft flight circles moved with the wind field. Important aspects of these data include the identification of mesoscale dynamic processes and aerosol effects on microphysical characteristics.

FORECAST MODEL EVALUATION

Data collected during DYCOMS II provides a natural basis for evaluating forecast products. Toward this end ECMWF and NCEP (AVN) model forecast calculations were archived for the entire month of July. Similarly, the Navy's Coupled Ocean/Atmosphere Mesoscale Prediction System (COAMPS) model was run with a relatively fine (6km) nested mesh centered on the target area. Output, and the initial data for these calculations was archived to allow subsequent sensitivity studies — with particular focii being the varying

---

[6]This material will appear outside of the main text of the article, sort of like a boxed inset

roles of model physics (especially microphysics) versus initialization on forecast quality. These data, when combined with archived remotely sensed data, *in situ* field data, and data of opportunity from buoys, ships and soundings define a small meso-scale network which will be invaluable in evaluating forecast bias from various models. Of particular note in this regard is that because of logistical constraints on night flying, flights during the DYCOMS-II field phase were not chosen based on meteorology. In addition the region of flight operations is largely dictated by controls on airspace and air-traffic lanes through restricted areas. Thus the flights are almost a random sample of conditions observed during the month.

Appendix A
Electronic Supplement [will not appear in print addition of article]— Flight Summaries

The experiment consisted of two basic flight patterns: entrainment and radar flight patterns. The entrainment flight patterns had a three-fold objective: to measure divergence and turbulent fluxes at various levels and characterize the mean states of both the boundary layer and the overlying air column. To achieve these objectives, the basic entrainment flight plan consisted of stacks of 30 minute (approximately 60 km diameter) circles. In contrast the objective of the radar flights was to characterize the evolution of a specific convective cell. For this reason, the radar flights consisted of shorter (6 minute) legs that attempted to fly over or through a specific point in the flow along varied headings.
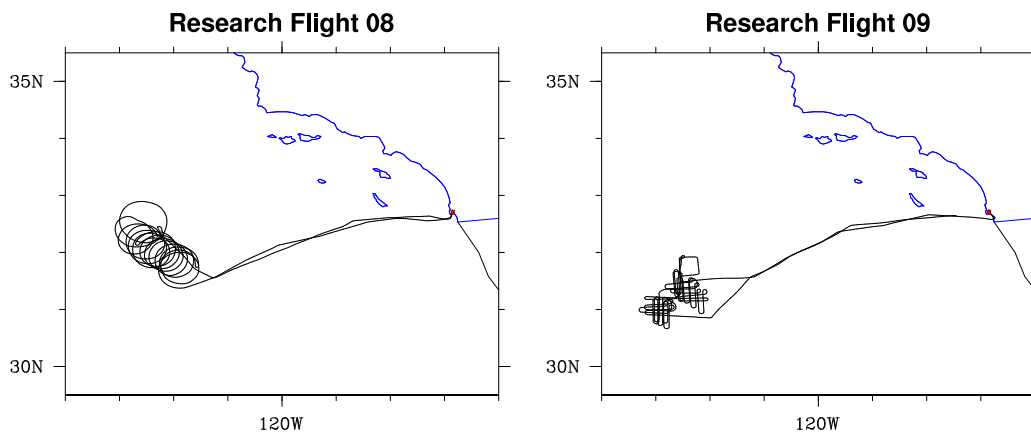

Figure 9: Flight tracks for RF08 and RF09, note the center of the circles drift with the mean northwesterly winds.

These differences between the two types of flight patterns are shown in Fig. 9. There were only two radar flights, RF09 and RF06, and although the flight tracks were not identical between the two, the idea was similar. The general nature of all the entrainment flights was identical, the only difference being in the ordering of the legs, and the transitions between circles. In general two opposing circles[7] were flown consecutively at each altitude, thus yielding an hour at any given level. On some flights, however, either the subcloud or surface layer circles were performed in only one direction in order to make time for other maneuvers. In addition, the entrainment flights allowed time for one leg whose objective was determined on a flight-by-flight basis. Typically this leg was a porpoising maneuver to obtain numerous penetrations through the entrainment region at cloud top. Lastly, flight maneuvers for calibrating air motion sensing were performed twice during the experiment — once on the third test flight, which took place on station during the day on July 7, 2001, and once on the outbound Ferry of RF07. The remainder of this summary focuses on the entrainment flight plans.

Fig. 10 illustrates how legs and profiles were distributed in the time-height plane. The circular legs are annotated and described in Table 1. Although none of the entrainment flights followed this plan exactly, the essential elements were conducted on each flight. Flights differed in the ordering, heading-sequence, and duration of the level legs, the exact position of the soundings, and the nature or the existence of the optional leg (which in the figure is indicated as a see-sawing, or porpoising leg, that repeatedly profiles the cloud top region). But each flight had four flux legs of at least 30 minutes at roughly the indicated heights, three radar/lidar legs at approximately the indicated heights, and from four to five soundings dispersed throughout

---

[7]Circles were flown by changing the aircraft heading at a constant rate in time, $12°$ min^{-1} for 30 min circles, thus defining circles with respect to the mean flow.
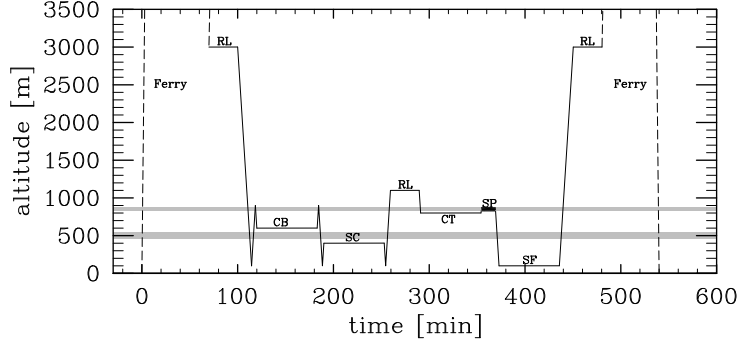
Figure 10: Time-Height cross section for basic entrainment flight plan. Approximately 410 minutes are spent in the target area. Shaded bars denote cloud top and base.

the time in the study area.

Table 1: Description of flight legs in basic entrainment flight plan. Here CW denotes a clockwise circle, CCW a counter clockwise circle.

Leg	Duration	Heading	Description
RL1	30 min	CW	Radar/Lidar and Dropsonde Leg at 3km
CB	60 min	CW-CCW	Level flux leg just above cloud base (CB)
SC	60 min	CCW-CW	Level flux leg in subcloud (SC) layer
RL2	30 min	CW	Radar/Lidar leg just above lidar dead-zone
CT	60 min	CW-CCW	Level flux leg just below cloud top (CT)
SP	30 min	CCW	Special (SP) Leg, generally porpoising at cloud top
SF	60 min	CCW-CW	Surface (SF) Leg at lowest safe flight level
RL3	30 min	CCW	Radar/Lidar and Dropsonde Leg at 3km

A basic summary of the conditions encountered on each flight is included in Table 2. Because the time on target approached seven hours, and the flight legs generally drifted with the mean wind (e.g., see the evolution of consecutive circles in Fig. 9) the actual area sampled by the aircraft was approximately 3000 km^2. For measurements of sea-surface temperatures (SSTs), tabulated from surface legs flown near the end of the time in the study area, this leads to a systematic high bias. For other quantities, the means can mask considerable time variability — this was perhaps most important for estimates of cloud base, which on some flights changed systematically through the course of the time in the study area by as much as 150 m. Among the flights the depth of the STBL varied by nearly a factor of two, with similar variations in cloud liquid water, thickness and wind speeds. Precipitation, as measured by the maximum radar reflectivity, was even more varied, with cloud layers ranging from essentially non ($Z < -15$ dBZ), to heavily (at least for stratocumulus, i.e., $Z > 0$ dBZ) precipitating.

For reference in analyzing the flight data in tables A-A the time-offset (time in seconds from the beginning of the data record) for the level legs and soundings are tabulated for the seven entrainment flights. Satellite conditions as observed from the GOES satellite for the nine flights are shown in Fig. 11. Snapshots in this figure are from the end of each flight for the nocturnal, and at the beginning of each flight for the diurnal flights. Note the generally widespread uniform marine stratocumulus cloud cover.
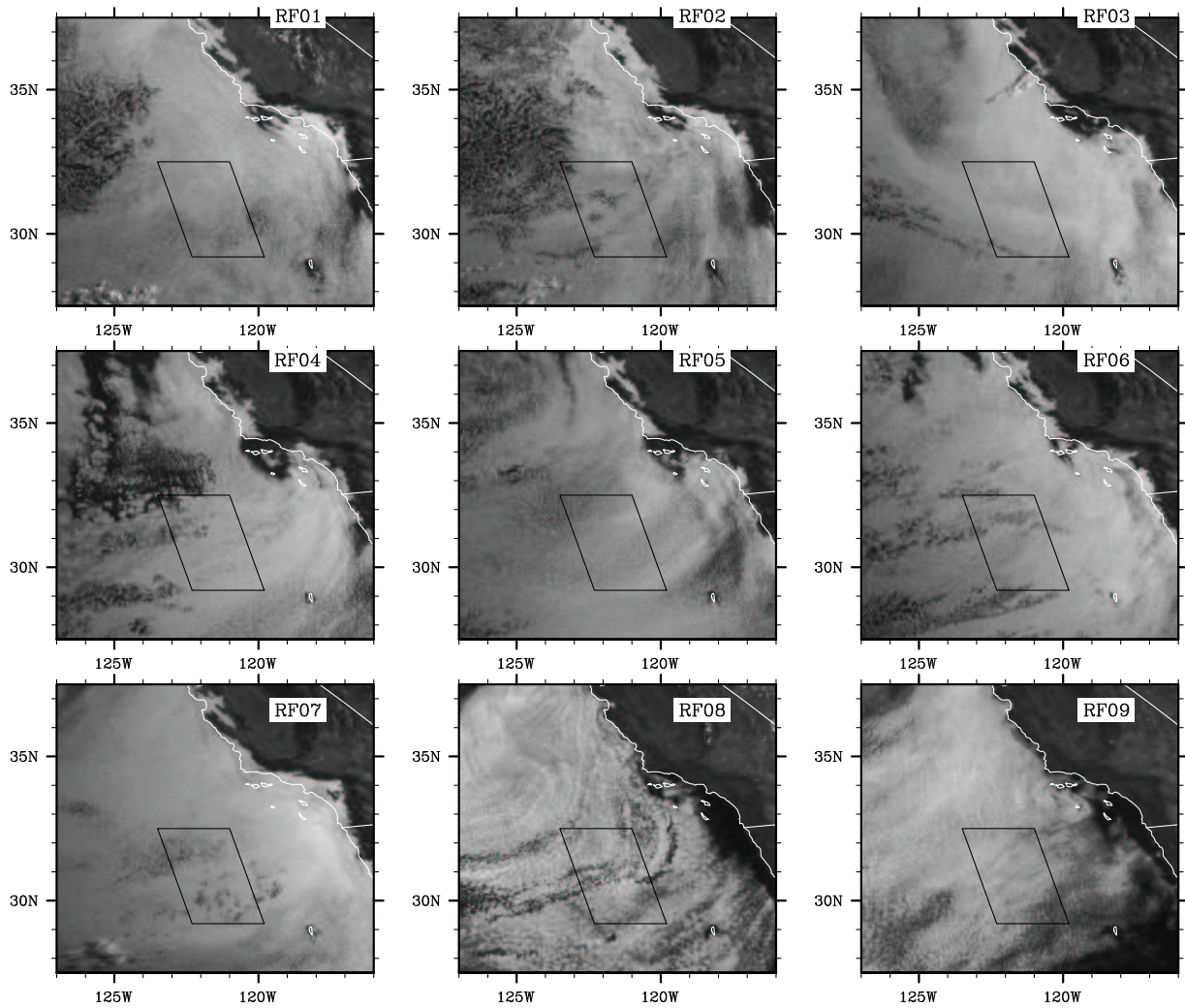
23

Figure 11: GOES visible imagery for flights DYCOMS-II research flights (nine panel figure, with each panel similar to Fig.3 to be added in subsequent draft).

Table 2: Summary of DYCOMS-II flights, July 2001. State variables are estimated from subcloud legs, SSTs are estimated from radiometric measurements during low altitude ($<$ 100 m) surface legs. Cloud base taken from average LCL for all legs within PBL. The cloud top liquid water $\overline{q}_{l,max}$ estimated from soundings. Flight latitude and longitude is at the center of flight region for middle four hours on target.

Flight	1	2	3	4	5	6	7	8	9
Take-Off[a]	06:01	06:24	06:18	06:22	06:19	05:39	05:53	19:45	18:16
Land	15:18	15:53	15:46	15:32	15:41	15:13	15:49	05:21	03:45
Date[b]	10	11	13	17	18	20	24	25	27
Latitude	31.3	31.4	31.0	29.7	30.5	30.6	31.3	32.1	31.2
Longitude	-121.7	-121.7	-121.6	-121.5	-121.7	-122.0	-121.4	-122.4	-122.7
SST	19	19	19	20	19	n/a	19	18	n/a
Wind Speed [ms^{-1}]	8	8	12	6	10	8	7	5	5
Wind Dir [°N]	324	310	300	274	287	340	326	319	345
Cloud Top [m]	850	800	700	1075	925	600	825	600	600
Cloud Base [m]	585	440	310	610	650	200	310	270	300
$\overline{\theta}_l$ [L]	289	288	288	289	288	288	288	289	288
$\overline{q}_t$ [gkg^{-1}]	9	9	10	9	8	9	10	10	10
$\overline{q}_{l,max}$ [gkg^{-1}]	0.6	0.6	0.7	0.9	0.6	0.7	0.9	0.6	0.6
Z [dBZ]									
N [cm^{-3}][c]	n/a	n/a	207	168	151	100	116	110	165
CCN[d] [cm^{-3}]	$160s^{0.4}$	$60s^{0.2}$	$300s^{0.8}$	$210s^{0.3}$	$210s^{0.3}$	$180s^{0.5}$	$140s^{0.4}$	$130s^{0.4}$	$290s^{0.3}$
CN [cm^{-3}]	274	290	472	290	417	389	281	245	558

[a]UTC, local time (PDT) plus seven hours

[b]at take off

[c]For flights RF01 and RF02 these numbers are taken from the SSP-100, for flights RF03-RF09 they are based on data taken with the Fast-FSSP

[d]The coefficients in this expression are derived by fitting data from a static CCN instrument to the form $N = Cs^k$. Relative errors in C and k are $\pm 25\%$ and $\pm 35\%$ respectively.

Table 3: Offset times for flight segments for RF01-RF03. RL denotes remote sensing leg; CB, cloud base leg; SC, subcloud leg; CT, cloud top leg; SP, special pattern (which varied from flight to flight); SF, surface flux leg. For the profiles we label full profiles (FP), cloud profiles (CP) and inversion profiles (IP).

#	GALT [m]	Time [s]	Type		#	GALT [m]	Time [s]	Type
RF01 Legs					RF01 Profiles			

| \multicolumn{4}{RF01 Legs} | | \multicolumn{4}{RF01 Profiles} |

RF01 Legs:

#	GALT [m]	Time [s]	Type
1	3248 ± 3.7	5550 - 7450	RL
2	625 ± 4.2	8400 -10200	CB
3	637 ± 3.5	10500 -12200	CB
4	481 ± 3.6	12400 -14200	SC
5	492 ± 4.3	14320 -16200	SC
6	758 ± 3.3	16600 -18200	CT
7	755 ± 3.2	18500 -20150	CT
8	1056 ± 2.9	20700 -22400	RL
9	924 ± 7.0	22650 -22950	SP
10	152 ± 3.2	23420 -25020	SF
11	96 ± 6.4	25200 -27000	SF
12	1893 ± 3.2	27400 -29200	RL

RF01 Profiles:

#	GALT [m]	Time [s]	Type
1	3246 - 183	7490 - 8005	FP
2	183 - 643	8005 - 8110	FP
3	616 - 892	10233 -10310	CP
4	892 - 615	10310 -10426	CP
5	494 - 915	16210 -16327	CP
6	915 - 750	16327 -16393	CP
7	750 - 166	20155 -20419	CP
8	166 - 1074	20419 -20584	FP
9	1050 - 761	22465 -22544	IP
10	761 - 945	22544 -22608	IP
11	935 - 149	22955 -23168	FP
12	113 - 1920	27060 -27300	FP

RF02 Legs:

#	GALT [m]	Time [s]	Type
1	2598 ± 4.1	5520 - 7495	RL
2	485 ± 3.9	8900 -11180	CB
3	517 ± 3.2	11260 -12380	CB
4	271 ± 4.8	12860 -14750	SC
5	271 ± 3.8	14900 -16640	SC
6	674 ± 4.5	16975 -18900	CT
7	674 ± 3.2	19020 -20840	CT
8	1117 ± 3.8	21560 -23120	RL
9	761 ± 4.6	23300 -25100	SP
10	107 ± 5.1	25500 -27440	SF
11	2530 ± 3.0	27860 -29660	RL

RF02 Profiles:

#	GALT [m]	Time [s]	Type
1	2601 - 194	7502 - 8013	FP
2	194 - 817	8013 - 8151	FP
3	765 - 431	8349 - 8471	CP
4	520 - 757	12422 -12470	CP
5	758 - 198	12469 -12608	FP
6	166 - 790	16750 -16854	FP
7	678 - 181	20841 -21020	FP
8	838 - 84	25177 -25468	FP
9	102 -2494	27479 -27804	FP

RF03 Legs:

#	GALT [m]	Time [s]	Type
1	2620 ± 8.4	2130 - 2860	RL
2	2613 ± 3.3	3140 - 6940	RL
3	377 ± 4.2	7657 - 9330	CB
4	378 ± 5.0	9450 -11192	CB
5	192 ± 4.4	11462 -13332	SC
6	527 ± 4.7	13537 -15380	CT
7	527 ± 3.3	15500 -17262	CT
8	1092 ± 2.4	17723 -19523	RL
9	370 ± 4.3	21992 -23792	SC
10	97 ± 3.5	24107 -25750	SF
11	98 ± 4.3	25900 -27657	SF
12	2547 ± 3.6	28012 -29898	RL

RF03 Profiles:

#	GALT [m]	Time [s]	Type
1	2612 - 164	7033 - 7455	FP
2	164 - 414	7455 - 7532	SP
3	378 - 735	11247 -11317	CP
4	735 - 176	11317 -11452	FP
5	194 - 743	13332 -13445	FP
6	743 - 516	13445 -13531	CP
7	527 - 168	17315 -17425	FP
8	162 -1118	17450 -17603	FP
9	1093 - 561	19573 -19743	FP
10	687 - 233	21454 -21662	FP
11	233 - 179	21662 -21705	SP
12	370 - 80	23782 -23880	SP
13	104 -2516	27710 -27992	FP

Table 4: Offset times for flight segments for RF04 and RF05

RF04 Legs					RF04 Profiles			
#	*GALT* [m]	*Time* [s]	Type		#	*GALT* [m]	*Time* [s]	Type
1	2582 ± 4.2	4682 - 6757	RL		1	2549 - 183	6770 - 7395	FP
2	676 ± 3.8	7807 - 9800	CB		2	183 - 1026	7395 - 7705	FP
3	677 ± 5.3	9970 - 11850	CB		3	1027 - 683	7703 - 7814	CP
4	368 ± 4.0	12347 - 14100	SC		4	679 - 1115	11844 - 11940	CP
5	370 ± 4.6	14210 - 16047	SC		5	1115 - 181	11940 - 12250	FP
6	1304 ± 2.7	16562 - 18172	RL		6	170 - 1218	16097 - 16362	FP
7	949 ± 3.4	18337 - 20100	CT		7	1301 - 933	18174 - 18326	IP
8	947 ± 3.1	20272 - 22072	CT		8	1135 - 99	23750 - 24150	FP
9	Porpoising	22132 - 23797	SP		9	105 - 2560	26345 - 26685	FP
10	101 ± 3.6	24172 - 26342	SF					
11	2518 ± 4.3	26712 - 28547	RL					

RF05 Legs					RF05 Profiles			
#	*GALT* [m]	*Time* [s]	Type		#	*GALT* [m]	*Time* [s]	Type
1	2578 ± 4.2	4638 - 6473	RL		1	2572-158	6478-6858	FP
2	728 ± 3.5	7412 - 8850	CB		2	158-975	6858-7068	FP
3	728 ± 3.5	8980 - 10766	CB		3	975-646	7080-7168	CP
4	357 ± 3.4	11300 - 12840	SC		4	729-1020	10763-10830	CP
5	355 ± 3.4	12970 - 14700	SC		5	1020-154	10830-11027	FP
6	1007 ± 2.4	15158 - 16808	RL		6	154-396	11028-11088	SP
7	782 ± 3.1	17330 - 18680	CT		7	356-172	14759-14805	SP
8	784 ± 3.1	18920 - 20630	CT		8	136-1025	14824-14969	FP
9	Porpoising	20656 - 22349	SP		9	1010-736	16801-16880	IP
10	752 ± 4.7	22463 - 24083	CT		10	755-108	24078-24267	FP
11	100 ± 4.6	25043 - 27028	SF		11	99-2570	27023-27273	FP
12	2526 ± 4.4	27348 - 28838	RL					

Table 5: Offset times for flight segments for RF07 and RF08

RF07 Legs

#	*GALT* [m]	*Time* [s]	Type
1	2613 ± 2.4	7423 - 9618	RL
2	446 ± 5.0	10690 - 12490	CB
3	450 ± 3.4	12600 - 14400	CB
4	231 ± 3.7	14770 - 16570	SC
5	228 ± 3.5	16741 - 18541	SC
6	1070 ± 3.1	18788 - 20598	RL
7	712 ± 4.4	20708 - 22508	CT
8	677 ± 5.1	22708 - 24500	CT
9	Porpoising	24773 - 25718	SP
10	90 ± 4.3	26050 - 27750	SF
11	100 ± 3.2	27990 - 29790	SF
12	2553 ± 4.1	30190 - 32010	RL

RF07 Profiles

#	*GALT* [m]	*Time* [s]	Type
1	2621 - 145	9614 - 10187	FP
2	145 - 920	10187 - 10473	FP
3	921 - 426	10472 - 10680	CP
4	444 - 973	14400 - 14515	CP
5	973 - 158	14515 - 14683	FP
6	144 - 1090	18563 - 18758	FP
7	1071 - 706	20597 - 20728	IP
8	679 - 140	24501 - 24628	SP
9	140 - 919	24628 - 24809	FP
10	902 - 85	25641 - 25915	FP
11	97 - 2564	29796 - 30127	FP

RF08 Legs

#	*GALT* [m]	*Time* [s]	Type
1	5695 ± 5.3	5839 - 7680	RL
2	437 ± 1.9	9158 - 10908	CB
3	472 ± 2.2	11000 - 12824	CB
4	135 ± 2.4	13184 - 14924	SF
5	255 ± 2.2	15043 - 16938	SC
6	1067 ± 2.9	17378 - 19058	RL
7	Porpoising	19199 - 20999	SP
8	90 ± 2.9	21195 - 23013	SF
9	275 ± 2.9	23273 - 24908	SC
10	495 ± 2.6	25238 - 26908	CB
11	524 ± 2.9	27112 - 28417	CT
12	2583 ± 3.3	28838 - 32338	RL

RF08 Profiles

#	*GALT* [m]	*Time* [s]	Type
1	5694 - 136	7675 - 8741	FP
2	136 - 569	8741 - 8848	FP
3	604 - 417	8923 - 9053	CP
4	467 - 640	12818 - 12908	CP
5	637 - 126	13003 - 13168	FP
6	253 - 61	16942 - 16997	SP
7	61 - 913	16997 - 17172	FP
8	1068 - 476	19059 - 19182	IP
9	542 - 94	21016 - 21177	FP
10	269 - 720	24903 - 25038	CP
11	720 - 499	25038 - 25113	IP
12	526 - 185	28418 - 28485	SP
13	185 - 2606	28485 - 28818	FP

Appendix B
Electronic Supplement [will not appear in print addition of article]— Instrumentation

Another very important component of the DYCOMS-II strategy was the instrument package. Excepting remotely sensed data from satellites, and other data of opportunity, all the instrumentation was carried by a single platform — the NSF/NCAR C130. The placement of various instruments or inlets on the aircraft is illustrated in Figs. 12 and 13. Unless otherwise stated all instruments recorded their measurements on the primary aircraft data system, thus ensuring precise temporal synchronization. The performance and details of these instruments is discussed further below.
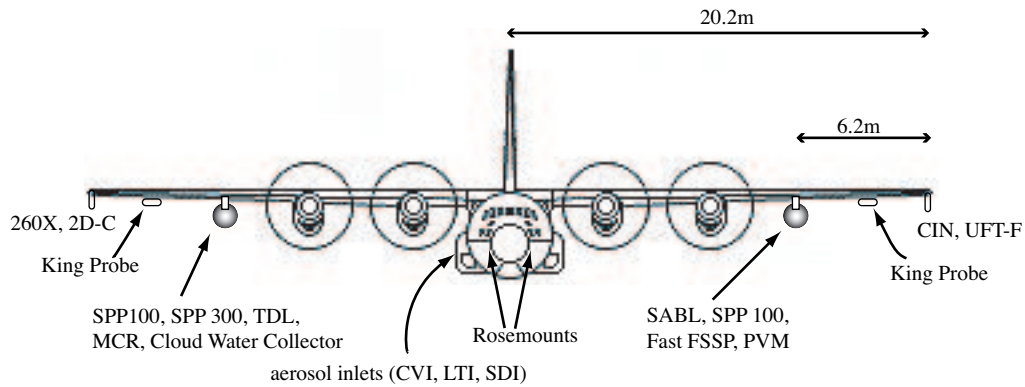

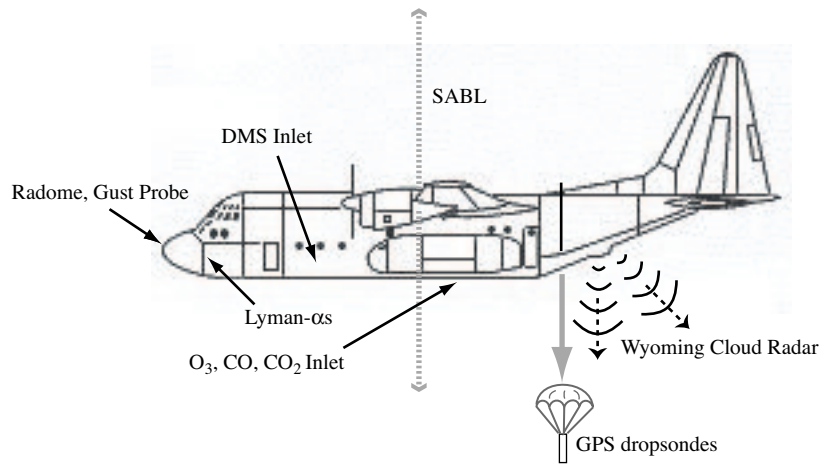Figure 12: Front view of C130 and Probe Locations.

Figure 13: Side view of C130.

a. Wind and turbulence measurement

The NCAR C-130 incorporates three primary systems into the measurement of a three-dimensional wind vector:

- the inertial reference system (IRS) measures attitude angles (pitch, roll and yaw or azimuth), accelerations and position of the aircraft in an earth based reference frame;

29

- the Global Positioning System (GPS) receiver measures the aircraft velocity and position in an earth based coordinate system using a constellation of satellites;

- the "radome gust probe" measures the atmospheric wind relative to the aircraft using a cruciform array of five pressure ports on the C-130 nose radome coupled to differential and absolute pressure sensors.

The wind measured relative to the aircraft coordinate system is combined with the motion of the aircraft relative to the earth coordinate system to yield a three-dimensional wind vector in meteorological coordinates. The mechanization equations and coordinate transformation matrices are detailed in Lenschow, D.H., 1986[8]

1) INERTIAL REFERENCE SYSTEM

The C-130 uses a Honeywell Laseref II SM strapdown ring laser gyro IRS[9] mounted in the cabin near fuselage station 240. The IRS provides position (latitude, longitude) initial accuracy of 0.8 nmi (with increasing uncertainty by 0.8 nmi per hour thereafter), pitch and roll accuracy to 0.05 degrees rms and azimuth (true heading) accuracy of 0.4 degrees rms. The primary source of error is the Schuler oscillation, a slowly varying drift in position and velocity measurements with a period of 84 minutes. The IRS has excellent short-term relative accuracy and resolution and its measurements are combined with the GPS, which has excellent absolute accuracy to provide a high resolution, high rate absolute accuracy measurement of aircraft position and velocity.

2) RADOME GUST PROBE

The radome gust probe measures the attack and sideslip (incident) flow angles of the aircraft and the dynamic pressure used in calculating the aircraft true airspeed. Five small pressure taps are drilled into the existing radome and tubing is routed to pressure transducers. The radome system[10], once calibrated for a specific aircraft, makes high accuracy wind and turbulence measurements at scales larger than the characteristic dimension of the aircraft. In the case of the C-130, the relevant scale value is the fuselage diameter, which measures 3.5 meters.

3) GLOBAL POSITIONING SYSTEM RECEIVER

The C-130 uses a Trimble TANS III six-channel GPS receiver that provides measurements of aircraft position, velocity and time at a one-second update rate. The accuracies of the measurements are 16 m rms horizontal, 25 m rms vertical and 0.25 m/sec for the velocities. Principles of the NAVSTAR GPS navigation can be found in Kayton and Fried.

b. Temperature measurements

1) ROSEMOUNT TOTAL TEMPERATURE PROBES

Temperature probes Rosemount total temperature probes The NCAR C-130 has redundant Rosemount model 102EAL total temperature probes and one Rosemount 102DB1CB deiced total temperature probe

---

[8]Aircraft measurements in the boundary layer. *Probing the Atmospheric Boundary Layer,* D.H. Lenschow, Ed., Amer. Meteor. Soc., 39-55, see also Lenschow, D. H., 1972: The measurement of air velocity and temperature using the NCAR Buffalo aircraft measuring system. NCAR Tech. Note/EDD-74,39pp.

[9]Kayton, M., and W.R. Fried, 1997: *Avionics Navigation Systems.* Wiley, New Yourk, N.Y., 773 pp.

[10]Brown, E.N., C.A. Friehe, and D.H. Lenschow, 1983: The use of pressure fluctuations on the nose of an aircraft for measuring air motion. *J. Clim. Appl. Meterol.,* **22,** 171-180.

[Total temperature sensors, 1963. Rosemount Engineering Company, Bulletin 7637]. These are platinum resistance wire probes with a nominal resistance of 50 ohms at $0°$ C. "Total temperature" refers to the temperature measured when the air is brought to rest without the removal or addition of any heat. The housing for the platinum element is designed to be in the airstream and slow the air to achieve the maximum temperature rise due to adiabatic heating. The degree to which a sensor measures the total temperature is called the "recovery factor". An ideal sensor has a recovery factor of 1.00. For the NCAR C-130 probes it is 0.95. For deiced temperature probes there is an additional correction of $0.2°$ C at sea level due to the deicing heat. Total temperature is relatively insensitive to location on the aircraft as long as it is outside the aircraft boundary layer[11].

Sensor wetting in clouds and precipitation affect temperature sensor accuracy. At times the sensor is only partially wet so a correction as depicted by a wet adiabatic process becomes questionable, and at 100 m/sec the difference can be as much as $2°$ C between wet and dry bulb temperatures in a saturated environment.[12]. Another potential problem in the marine boundary layer is the accumulation of sea salt on the sensor element[13].

The accuracy of these probes is better than $0.5°$ C in cloud free air as demonstrated by aircraft intercomparisons and tower fly-by calibrations. An "airspeed maneuver" where the aircraft airspeed is varied over the range of research airspeeds while maintaining altitude can also be used to estimate and verify the errors and corrections due to heating effects. The frequency response is less than 10Hz[14]. Corrections for dynamic heating and deicing are described in RAF Bulletin #9 , http://raf.atd.ucar.edu/Bulletins/bulletins.html

The location of the Rosemount temperature probes is depicted in figure 12. The deiced probe (not shown) is just outboard of the left pod underneath the wing about 10" from the leading edge.

2) UFT

A specially designed version of the Ultra Fast Thermometer UFT-F (Haman et al., 1997) with two temperature sensors was prepared for DYCOMS II experiment. The UFT is a platinum resistance thermometer shielded from cloud drops by an upstream obstacle and stregthened by a tungsten coating. An advantage of the UFT-F is that it allows measurements of temperature at centimeter resolution (time constant about 10^{-4} s, signal recorded at 1kHz and selected segments recorded at 10kHz). The UFT-F was originally to be mounted under the pod on the left wing of NCAR C-130 aircraft, close to the Fast FSSP and PVM probes; due to technical limitations the probe had to be moved to the tip of the left wing, six meters from the other fast probes. This wing-tip location caused troubles during the experiment: intensive vibration (apparent resonance) at ferrying speeds and altitudes resulted in sensor failures. Extensive data was only collected during RFO3 and RF05, although limited data is also available on some other flights.

---

[11]Cooper, W.A., D. Rogers, 1991:Effects of airflow trajectories around aircraft on measurements of scalar fluxes. *J. Atmos. Oceanic Technol.,* **8,** 66-77.

[12]Lenschow, D.H., W.T. Pennell, 1974. On the measurement of in-cloud and wet-bulb temperatures from an aircraft. *Mon. Weather Rev.,* **102,** 447-454

[13]Friehe, C.A., 1986. Fine scale measurements. *Probing The Atmospheric Boundary Layer,* D.H. Lenschow, Ed., Amer. Meteor Soc., 29-38.

[14]Spyers-Duran, P. and D. Baumgardner, 1983: In flight estimation of time response of airborne temperature sensors. *Preprints Fifth Symp. On Meteorological Observations and Instrumentation*, Toronto, Amer. Meteor. Soc., 237-255.

c. Water vapor

1) DEW POINT HYGROMETERS

Two General Eastern Model 1011B hygrometers are routinely flown on the NSF/NCAR C-130 for the purpose of obtaining airborne measurements of dew and frost point temperatures. As stated by the instrument manufacturer, these sensors are capable of measuring dew/frost points between -75° C and +50° C over a wide range of temperatures, pressures, and airspeeds.

The General Eastern hygrometers operate on the chilled-mirror principle. Under this method, a mirror is thermoelectrically cooled until it reaches a temperature at which condensation begins to form. The mirror is then held at that temperature, and the presence of condensation is sensed optically. The signal output from the instrument is a voltage corresponding to the temperature of the mirror.

The accuracy of the measurements obtained from the General Eastern hygrometers is a function of the dew point temperature. At a dew point temperature of -75° C, the error in the measurements is approximately +1.0° C. At a dew point temperature of +50° C, the associated error is approximately +0.25 ° C. The response time of the hygrometers is variable and is dependent on the dew point, the slew rate, and the flow rate and thickness settings for the sensor. At higher dew points and moderate depressions (with depression taken as the temperature difference between the mirror and the sensor body), the response time is typically 1° C per second. At lower dew points and/or larger depressions, the response time can - at the upper limit - be reduced to tens of minutes. These slower response times at low dew point values are also partly attributable to the reduced availability of water molecules and the resulting slow crystal growth rate. The slower response of the General Eastern hygrometers at lower dew points has, in fact, been routinely observed by the RAF. When operated in regions of the atmosphere (i.e., higher altitudes) where the ambient temperature is colder and dew point temperatures are lower, the signals from the General Eastern hygrometers on the C-130 display a much slower response and also exhibit marked oscillatory behavior.

It has been the experience of the RAF that mixing ratio values derived from the General Eastern hygrometer data show periodic "overshooting" and offsetting from mixing ratio data obtained from the RAF Lyman-alpha hygrometers. This problem typically occurs in more humid atmospheric environments and is attributable to temporary saturation of the General Eastern sensors. Thus, for those cases in which the C-130 is flying in high humidity environments, users of RAF data sets are advised to rely on collected Lyman-alpha data for mixing ratio measurements.

2) FAST RESPONSE HYGROMETERS

Two Lyman-α probes a new laser-hygrometer (the tunable diode laser, TDL) and chilled mirror devices were used to estimate water-vapor mixing ratios. One Lyman-α was a cross-flow instrument that had a slightly slower response, but performed better in cloud, both Lyman-α probes were calibrated on the fly by slaving them on long-timescales to the chilled mirror dew point hygrometers. Initial examinations of the data indicated that the cross-flow instrument performed more reliably. The TDL is an open path instrument that scans a water-vapor spectral line near 1.37 μm [R. May, JGR, Vol 103, 19,161-19,172, 1998]. Test flights indicated that it performed better than the Lyman-α probes in cloud, although its performance is still being evaluated. While in the past the TDL has been sampled at 1 s^{-1}, for DYCOMS-II it sampled the flow at a variety of rates, at times making an independent measurement every 128 ms.

d. Trace gas measurements (CO$_2$, CO, O$_3$, DMS)

To measure *in situ* CO$_2$, a commercial non-dispersive infrared analyzer was modified to implement temperature and pressure control after the manner of Boering, et al. [GRL, 21, 2567-2570, 1994]. Because the

NCAR instrument was developed for tropospheric measurements, water was removed from ambient samples using a Nafion dryer and a $MgClO_4$ desiccant trap. The instrument had a precision of 0.1 ppbv for a 10s averaging time and an accuracy of ± 0.4 ppbv.

CO was measured using a commercially available instrument based on the principle of vacuum UV resonance fluorescence, as published by Gerbig, et al. [JGR, Vol. 104, No. D1, 1699-1704, 1999]. The instrument had a 3 ppbv detection limit, for a 0.06s averaging time, with an accuracy of +/- 3 ppbv.

Two methods were utilized to measure ozone. The first was based on UV absorption, and had a 0.1 Hz sample rate and a 1 ppbv detection limit. A fast-response instrument was also deployed, using the chemiluminescent reaction with NO to quantify ozone. This instrument exhibited a 3 Hz frequency response and a 0.2 ppbv detection limit.

Atmospheric pressure ionization mass spectrometry (APIMS) was used to measure DMS. In this implementation of APIMS, the reagent ion H3O+ is formed from primary ions from ionization of nitrogen and water vapor (H2O) by a nickel-63 beta emission. The monitored ion is DMSH+, which is formed from the reactions of DMS with H3O+. Our use of APIMS includes the continuous addition of high isotopic purity d3-DMS as an internal standard. This results in high precision of the measurements and also allows unambiguous determination of the sensitivity of the technique as atmospheric conditions vary. During DYCOMS II the DMS measurements were made by sampling for ambient DMS for 20 milliseconds followed by 20 milliseconds of the DMS standard to yield a net sampling rate of 25 Hz (samples/sec). The detection limit is estimated to be 1 pptv for a 1 second integration.

e. Particle Inlets

Inside the cabin of the cabin of the C-130 was a wide variety of instrumentation for measuring aerosol particles in real time and for collecting particles for later analyses. Four inlets were used to bring ambient air samples inside the cabin for particle measurements: LTI, SDI, CVI, and CN-cone. The LTI and SDI were operated iso-kinetically (velocity at the inlet tip matched the airspeed) so that ambient concentrations of large particles ($> 1\mu$m) are preserved.

The Low Turbulence Inlet (LTI) provided sample air to streaker and impactor instruments. The LTI uses boundary layer suction in the inlet tip to reduce the loss of large particles by turbulence. As a result, the concentration of large particles is enhanced in the core flow. LTI flows were controlled automatically to maintain isokinetic sampling at the inlet tip and to reduce turbulence in the diffuser inlet.

The Solid Diffuser Inlet (SDI) provided air for CCN, OPC and CN measurements, independent of the LTI. The SDI is a conical diffuser that decelerates the flow from 110 m s^{-1} to 4 m s^{-1}. Flow rates for isokinetic sampling with the SDI were calculated over a range of airspeeds typical for the C-130. Flow demands of the instruments were normally fixed, and isokinetic sampling was achieved for airspeeds 113 m s^{-1}. Non-isokinetic sampling occurred when the aircraft speed was different from this or during occasional interruptions for changing sample media or servicing instruments.

f. Aerosol Particle Collections

Aerosol particle samples were collected from the LTI, SDI, and CVI. Some particles were collected on Nucleopore filter substrate, while others were simultaneously impacted on electron microscope grids. The particle samples were analyzed for physico-chemical properties by scanning and transmission electron microscopy (SEM and TEM, respectively) and elemental single particle analysis methods[15]

---

[15]See Anderson, J.R., P.R. Buseck and R. Arimoto, 1996: Characterization of the Bermuda Aerosol by combined individual-particle and bulk-aerosol analysis, *Atmos. Environ.,* **30,** 319-338, and Twohy, C.H. and B.W. Gandrud, 1998: Electron microscope analysis of residual particles from aircraft contrails, *Geophys. Res. Lett.,* **25,** 1359-1362.

High volume air flow from the SDI fed a three-stage virtual impactor in which the concentration of particles was increased by a factor 23 into sequentially smaller flows. The final highly concentrated sample was collected on stretched teflon filters. This technique produces sufficient mass for sensitive analyses in a relatively short time. These teflon filter samples of submicron particles and some CVI droplet residue particles were analyzed for organic and inorganic functional groups by Fourier Transform Infrared (FTIR) spectroscopy[16] and for elemental analysis by X-ray Fluorescence (XRF).

g. *Microphysical and Particle Instrumentation*

1) LIQUID WATER PROBES

A great variety of probes were flown for estimating properties of particles (including cloud droplets) in the STBL. To estimate bulk properties of the cloud layer, such as liquid water two PMS-King Probes, and a PVM-100A were available. The King-probe is based on a hot wire technique which measures the liquid water concentration in the range of 0.05-3 g m^{-3}; it samples a volume of 4000 cm^{3}s^{-1} at 10 Hz. The PVM-100A is a very high rate instrument which uses a light scattering technique to estimate integrated droplet distribution volume and surface area for drops larger than 4μm diameter. This instrument samples a volume of 300 cm^{3}s^{-1} at a rate of up to 1000 samples per second. During flights RF01 and RF02 the PVM-100A sampled the flow at a rate of 250 sps, on subsequent flights it sampled at 1000 samples per second.

A complementary instrument, the Cloud Integrating Nephelometer (CIN) measures *in situ* the optical scattering coefficient of cloud particles with sizes over a range of about 5 to 2000 μm in diameter. Its sample volume is 0.3 m^{3}s^{-1} and data is sampled at a rate of up to 250 samples per second. Its sensitivity to a wide size range of particles covers the individual size ranges of other microphysics probes used on the C-130, such as the SPP-100 droplet probe and the 260X drizzle probe, making it possible to perform data consistency checks that may enhance data accuracy.

2) OPTICAL PARTICLE PROBES

To estimate the distribution of particles at a given size a number of techniques and probes were used as outlined in Table 6. The probes operated using one of several basic principles, single-particle scattering (sps) or shadowing of light. The scattering of the SPP-100 and Fast-FSSP is calibrated assuming water scatterers. the SPP-200 and SPP-300 are calibrated using beads with a refractive index of 1.59. The SPP family of probes is derived from earlier versions from Particle Measuring Systems (PMS), with upgraded electronics from Droplet Measurement Technologies.

3) RDMA:

The Radial Differential Mobility Analyzer (RDMA) measures the size distribution and concentration of particles in the size range 8-130nm diameter.[17] The technique is to put electrical charge on particles in the sample air and then to pass the sample through a small chamber that has a continuous flow of dry, particle-free sheath air. The flows of sample and sheath flow are precisely controlled at 8.3 and 83 cm^3 s^{-1}, respectively. Narrow size segments of the particles are extracted by imposing an electrical field perpendicular to the air flow, and these particles are passed to a CN counter. Every three minutes, the voltage cycles through a

---

[16]Allen, D.T., E.J. Palen, M.I. Haimov, S.V. Hering, and J.R. Young, 1994: Fourier-transform infrared-spectroscopy of aerosol collected in a low-pressure impactor (LPI/FTIR) - Method development and field calibration, *Aerosol Sci. Technol.,* **21,** 325-342

[17]For more information on the RDMA technique, see Russell, L.M., S-H. Zhang, R.C. Flagan, J.H. Seinfeld, M.R. Stolzenburg, R. Caldow, 1996: Radially classified aerosol detector for aircraft-based submicron aerosol measurements. *J. Atmos. Oceanic Techn.,* **13,** 598-609

Table 6: Instruments for in-situ measurements of cloud and aerosol particle size distributions.

Instrument	Range [μm]	Sample Volume [$\mathrm{cm^{-3}\,s^{-1}}$]	Principle	Feature	Operator
SPP-200	0.1 - 3	1	sps	10Hz, 30 ch	RAF
SPP-300	0.3 - 30	7	sps	10Hz, 30 ch	RAF
SPP-100	2 - 47	50	sps-water	10Hz, 40 ch	RAF
Fast-FSSP	5 - 44	50	sps-water	asynchronous 255 ch	Brenguier
PMS-260X	10 - 640	4000	shadow	10Hz, 60 ch	RAF
PMS-2DC	25 - 800	5000	shadow	10Hz, 32 ch	RAF

smooth exponential curve from 0v to -5000v and back to 0v. The time histories of particle counts, voltages, and flows are numerically inverted to generate up-scan and down-scan size distribution measurements, $dn/d\log D_p$ versus diameter D_p, in sixty-two bins. Size calibrations were done with 80nm monodisperse polystyrene latex spheres. Sample air for the RDMA came from the starboard side solid-diffuser inlet. The RDMA performed well during all of the DYCOMS-II flights. A new bulk cloud water collection system jointly developed at Colorado State University (CSU) and the National Center for Atmospheric Research (NCAR) was mounted on the starboard instrumentation pod (Fig. 12). It provided bulk cloud water samples for chemical characterization and cloud processing studies.

4)   CCN AND CN INSTRUMENTS

Two Wyoming CCN counters (WyoCCN) were flown during DYCOMS-II. WyoCCN is a static thermal-gradient diffusion chamber, taking a grab sample every 30s. Both, the top plate and the bottom plate of the chamber, are covered with water-saturated blotter paper. A temperature controller regulates the differential temperature between the plates, thus creating a supersaturation in the center of the chamber. Particles with critical supersaturation less than the controlled supersaturation activate and grow to the size of cloud droplets. These are illuminated by a laser and the scattered light intensity is recorded[18]. Both instruments measured CCN number concentration at supersaturations of 0.2%, 0.4%, 0.8%, and 1.6%. In addition, two continuous flow CN counters (TSI 3010 and TSI 3760) [19] measured the concentration of particles larger than 0.01 μm.

5)   CLOUD WATER COLLECTOR:

The cloud water collection system employs an axial-flow cyclone to separate cloud droplets from the ambient air stream. At flight speeds (110 $\mathrm{ms^{-1}}$), ram pressure drives air and cloud droplets into the 6 cm diameter inlet of the axial-flow cyclone. A stationary curved vane assembly redirects the incoming axially-directed flow to produce a rapidly rotating flow field. In this flow, centrifugal force rapidly moves entrained cloud droplets to the wall of the collector. Accumulated cloud water is drawn off the wall of the collector and directed to a sample storage system consisting of seven storage bottles that are filled sequentially during a flight. The entire cloud water collection system is housed in a Particle Measurement System (PMS) canister and is operated with a LabVIEW-based control and data acquisition system.

---

[18]For a detailed description of the WyoCCN instrument see Delene and Deschler, 2000: Calibration of a photometric cloud condensation nucleus counter designed for deployment on a baloon package, *J. Atmos. Oceanic Techno.,* **17,** 459-467

[19]TSI 3010 was operated by the University of Wyoming; TSI 3760 was operated by NCAR

A computational fluid dynamics (CFD) analysis of the axial-flow cyclone provided a prediction of collector performance, and indicated a 50% cut diameter of approximately 8 microns when operated at 115 m s^{-1}. Over the course of the project 54 samples were obtained. Sample pH was measured on site immediately following each flight, and the cloud water from each sample period was preserved on site for post-campaign analysis at CSU. Concentrations of major ions (Cl-, NO3-, SO42-, Na+, NH4+, K+, Ca2+ and Mg2+), peroxide, formaldehyde, S(IV), and trace metals have been measured. Preliminary analysis indicates that sodium and chloride were the two most abundant ions in every DYCOMS-II sample, accounting for approximately 2/3 of total ions in solution. Ratios of chloride, potassium, magnesium, and calcium to sodium show that these species were present in proportions similar to those found in sea water. Sulfate, nitrate, and ammonium had ratios that were higher than what would be expected in sea water, indicating that there were additional sources for these species in the remote marine environment.

6) COUNTERFLOW VIRTUAL IMPACCTOR (CVI):

The counterflow virtual impactor (CVI)[20] has been utilized both in the air and on the ground in studies of aerosol/cloud interactions, cloud physics, and climate. For DYCOMS, it was used to compare properties of material within droplets to properties of ambient aerosol particles in order to study which particles nucleate clouds and how clouds process particles. At the CVI inlet tip, cloud droplets larger than about 8 mm aerodynamic diameter were separated from the interstitial aerosol and impacted into dry nitrogen gas. This separation is possible via a counterflow stream of nitrogen out the CVI tip, which assures that only cloud droplets (with more inertia) are sampled. The water vapor and non-volatile residual particles remaining after droplet evaporation are sampled downstream of the inlet with selected instruments. In DYCOMS, these included a CN counter and optical particle counter to measure residual particle number and size distribution, electron microscope samples for single particle chemical analysis, filters for FTIR/XRF analysis of organic functional groups and elements, and a Lyman-alpha hygrometer for liquid water content.

h. Remote Sensors

1) WYOMING CLOUD RADAR (WCR):

The WCR[21] was operated with a dual antenna arrangement, one antenna pointing vertically down (the nadir beam), the other at a 38 degree backward slant in the plane defined by the aircraft axis and the nadir beam. The two antennas were used in a rapidly interleaved fashion. Data so obtained will yield dual-Doppler analyses. The radar was operated during all flights. The radar legs (RL in Table 3) flown not far above cloud top yielded full coverage from the ocean surface to the top of the cloud. Flight segments in and below the cloud layer provided partial views. Flight segments at altitudes > 2 km yielded poor data because of the loss in sensitivity with distance to the target.

The WCR spatial resolution is 30 m but the sampling/recording was done with 15 m spacing. The minimum detectable signal (with high signal to noise ratio) at 300 m distance to the target was about -26 dBZ. This sensitivity was sufficient to yield measurements even in the most tenuous of the clouds encountered during DYCOMS.

The WCR recorded data in over 90 % of the total flight times. In two flights (RF06 and RF09), the flight plan was designed to give maximum temporal resolution in repeated sampling of the same cloud volume.

---

[20]Noone, K.J., Ogren, J.A., Heintzenberg, J., Charlson, R.J. and D.S. Covert, Design and calibration of a counterflow virtual impactor for sampling of atmospheric fog and cloud droplets, Aer. Sci. Technol., 8, 235-244, 1988; Twohy, C.H., Schanot, A.J. and W.A. Cooper, Measurement of condensed water content in liquid and ice clouds using an airborne counterflow virtual impactor, J. Atmos. Oceanic Technol., 14, 197-202, 1997.

[21]For more info see http://www-das.uwyo.edu/ wcr

2) SABL (Scanning Aerosol Backscatter Lidar)

SABL is an elastic back-scatter lidar that was used to map atmospheric back-scatter and cloud edge structure. The lidar has a Nd:YAG laser as the source operating at 20 Hz and at two wavelengths: 1064 nm and 532 nm. SABL is mounted in an NCAR/RAF instrumentation pod on the left wing and is capable of looking vertically either up or down. The return signals from both wavelengths are digitized with a 12-bit digitizers at rates up to 40MHz. Cloud-top height is obtained from the remote sensing flight legs when the aircraft was more than 200 m from the cloud. Even though the detectors are saturated by the cloud return from close range, the range to the cloud-top or cloud-bottom can still be extracted from the return signal. Figure 14 is plot of cloud-top height vs time from RF03 during a remote sensing leg of the flight. Cloud-top information is obtained from individual profiles so the horizontal spacing between profiles is approximately 5 m. The 40 MHz digitization rate gives a vertical resolution of 3.75 m.
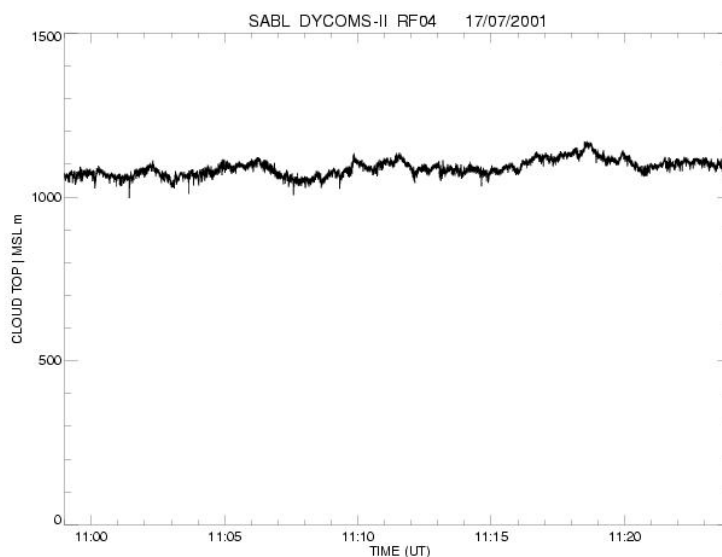

Figure 14: Cloud top derived from SABL on RF04

3) Multichannel Cloud Radiometer (MCR):

The MCR is a seven-channel radiometer that scans between $\pm$ 45 degrees about the flight track with a mirror scan rate of 3.47 revolutions/s. Data from each channel is simultaneously sampled with an overall rate of 5000 sps. Each active scan yields 360 samples (pixels), with pixel sizes depending on height above target; swaths widths are roughly twice the distance to the target. Since the scanning is continuous, the MCR produces a spectrally resolved image (see for instance Fig. 15) of features below the aircraft, including cloud tops, terrain, vegetation, pack ice, etc. Channel 7 (Table 7) is in the infrared and was hoped to provide nocturnal imaging of the cloud layer, however this channel did not function properly and images are limited to the daytime, and thus only the early morning periods at the end of nocturnal flights are available.

4) Pyrometers:

Two EG&G Heimann Optoelectronics radiation pyrometers are routinely deployed on the NSF/NCAR C-130 for the purpose of obtaining airborne surface temperature measurements. The RAF uses Heimann model KT 19.85 pyrometers (see specifications in Table 8, which operate in the spectral range of 9.6-11.5μm. The
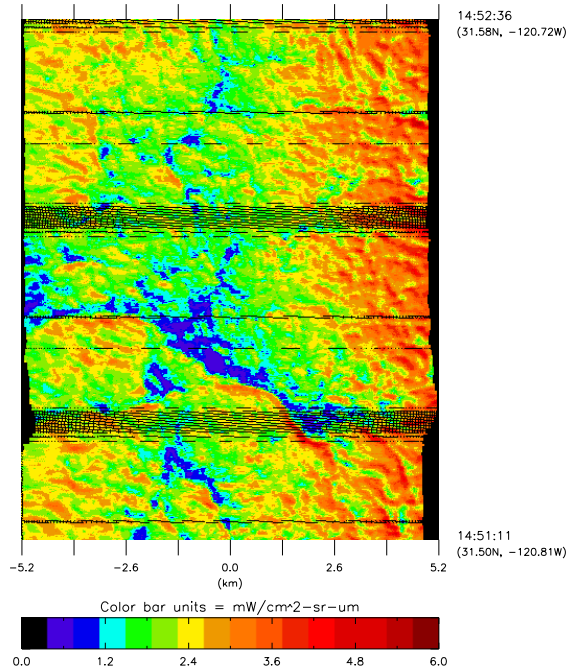
Figure 15: MCR Channel 4, from RF02

latter is a portion of the electromagnetic spectrum in which atmospheric transmission is high. Consequently, the KT 19.85 pyrometers are, for the most part, well suited for making surface temperature measurements on board research aircraft. Certain environmental effects can degrade the accuracy of surface temperature measurements obtained from Heimann pyrometers flown on aircraft. Specifically, potential errors can be introduced into surface temperature measurements obtained using these pyrometers by: 1) non-unity emittance and non-zero reflectance of the ground or sea surface being studied; 2) the emission of infrared (IR) radiation by water vapor in the atmospheric layer between the pyrometer and the surface. Additional discussion of these two phenomena and on the Heimann KT 19.85 pyrometers in general can be found in RAF Bulletin Number 25, Passive Broadband and Spectral Radiometric Measurements Available on NSF/NCAR Research Aircraft, which is available on-line at http://raf.atd.ucar.edu/Bulletins/bulletin25.html.

Calibration of the Heimann pyrometers is carried out periodically in the RAF calibration laboratory

Table 7: Specifications for MCR.

Channel	λ [μm]	$\Delta\lambda_{FWHM}$ [μm]	Application
1	0.640	0.063	τ and cloud mapping
2	0.761	0.001	
3	0.763	0.001	
4	1.06	0.07	r_e
5	1.64	0.05	phase
6	2.16	0.08	phase and particle size
7	10.9	0.9	Not operating

Table 8: Specifications for Heimann KT 19.85 Pyrometer.

Passband:	9.6–11.5 μm
Range:	-50–400°C
Resolution:	$\approx$ 1°C (depending on surface temperature)
Response Time:	0.3 s (adjustable)
Field of View:	2°

using an Eppley Laboratories, Inc. Infrared Blackbody Source Model BB16T. This blackbody target displays a temperature accuracy and uniformity of 0.1° C over a temperature range of 10 to +60°C and has an emissivity of 0.995.

5)   SATELLITES:

Various satellite data which was collected as part of the study is tabulated in Table 9.

Table 9: Satellite data sets.

Platform	Sensor Types	Data Types
GOES	Imager and Sounder	Binary data and images
NOAA	AVHRR,AMSU,HIRS,SSU,MSU	Binary data and images
DMSP	SSM/I and Visible/Infrared Sensor	Binary data and images
QuikSCAT	Scatterometer	Binary data
ERS-1	Scatterometer	Images
TRMM	Microwave Imager	Binary data
Terra	MODIS	Binary data